

# **DEVELOPMENT OF EFFICIENT COMPUTATIONAL METHODS FOR BETTER ESTIMATION OF OPTICAL PROPERTIES IN DIFFUSE OPTICAL TOMOGRAPHY**

A THESIS  
SUBMITTED FOR THE DEGREE OF  
**Doctor of Philosophy**  
IN THE FACULTY OF SCIENCE

by

**RAVI PRASAD K. J.**



IISc MATHEMATICS INITIATIVE (IMI)

Indian Institute of Science  
BANGALORE – 560 012

AUGUST 2013

©RAVI PRASAD K. J.

AUGUST 2013

All rights reserved

TO

My Family,

Specially to my brother *Guru*.

# Acknowledgements

Working on my Ph.D. dissertation made it clear to me that all scientific research is a synergistic product the interest and thinking of many people. I am grateful for all the wisdom of the researchers and also for sharing their knowledge and experience.

I am grateful to my advisor Dr. Phaneendra K. Yalavarthy and feel myself lucky to have him as my research advisor. Thanks to him for the arduous task of guiding me and also for emphasizing hard work whenever I showed signs of being distracted from my research work. I thank the faculty of the Supercomputer Education and Research Centre (SERC) and Department of Electrical Engineering for teaching and exposing me to their respective research areas.

I specially thank Jayaprakash for his sincerity and dedication towards his work which was a constant inspiration for me and also for fruitful discussions whenever I encountered doubts. I thank my friends other lab-mates Calvin Shaw, Kalyan Ram and Yamuna without whom I would not have a chance to complete my dissertation. I would like to thank all my other friends, to name a few, like Sainath, Appala Naidu, Samar Singh, Saurabh Gupta, I will always cherish their friendship and thank them for all the support and encouragement.

Last but not the least, I would like to thank my parents and brothers for their continuous support and help in handling the challenges during the preparation of this dissertation. I would like to express my sincere gratitude to all those who have directly or indirectly helped me.

# Abstract

Diffuse optical tomography (DOT) is one of the promising imaging modalities that provides functional information of the soft biological tissues in-vivo, such as breast and brain tissues. The near infrared (NIR) light (600-1000 nm) is the interrogating radiation, which is typically delivered and collected using fiber bundles placed on the boundary of the tissue. The internal optical property distribution is estimated via model-based image reconstruction algorithm using these limited boundary measurements.

Image reconstruction problem in DOT is known to be non-linear, ill-posed, and sometimes under-determined due to the multiple scattering of NIR light in the tissue. Solving this inverse problem requires regularization to obtain meaningful results, with Tikhonov-type regularization being the most popular one. The choice of the regularization parameter dictates the reconstructed optical image quality and is typically chosen empirically or based on prior experience. An automated method for optimal selection of regularization parameter that is based on regularized minimal residual method (MRM) is proposed and is compared with the traditional generalized cross-validation method. The results obtained using numerical and gelatin phantom data indicate that the MRM-based method is capable of providing the optimal regularization parameter.

A new approach that can easily incorporate any generic penalty function into the diffuse optical tomographic image reconstruction is introduced to show the utility of non-quadratic penalty functions. The penalty functions that were used include, quadratic ( $\ell_2$ ), absolute ( $\ell_1$ ), Cauchy, and Geman-McClure. The regularization parameter in each of these cases were obtained automatically using the generalized cross-validation (GCV) method. The reconstruction results were systematically compared with each other via

utilization of quantitative metrics, such as relative error and Pearson correlation. The reconstruction results indicate that while quadratic penalty may be able to provide better separation between two closely spaced targets, its contrast recovery capability is limited and the sparseness promoting penalties, such as  $\ell_1$ , Cauchy, Geman-McClure have better utility in reconstructing high-contrast and complex-shaped targets with Geman-McClure penalty being the most optimal one.

Effective usage of image guidance by incorporating the refractive index (RI) variation in computational modeling of light propagation in tissue is investigated to assess its impact on optical-property estimation. With the aid of realistic patient breast three-dimensional models, the variation in RI for different regions of tissue under investigation is shown to influence the estimation of optical properties in image-guided diffuse optical tomography (IG-DOT) using numerical simulations. It is also shown that by assuming identical RI for all regions of tissue would lead to erroneous estimation of optical properties. The a priori knowledge of the RI for the segmented regions of tissue in IG-DOT, which is difficult to obtain for the *in vivo* cases, leads to more accurate estimates of optical properties. Even inclusion of approximated RI values, obtained from the literature, for the regions of tissue resulted in better estimates of optical properties, with values comparable to that of having the correct knowledge of RI for different regions of tissue.

Image reconstruction in IG-DOT procedure involves reduction of the number of optical parameters to be reconstructed equal to the number of distinct regions identified in the structural information provided by the traditional imaging modality. This makes the image reconstruction problem to be well-determined compared to traditional under-determined case. Still, the methods that are deployed in this case are same as the one used for traditional diffuse optical image reconstruction, which involves regularization term as well as computation of the Jacobian. A gradient-free Nelder-Mead simplex method was proposed here to perform the image reconstruction procedure and shown to be providing solutions that are closely matching with ones obtained using established methods. The proposed method also has the distinctive advantage of being more efficient due to being regularization free, involving only repeated forward calculations.



# **Keywords**

Medical imaging, biomedical optical imaging, diffuse optical tomography, dynamic diffuse optical imaging, inverse problems, regularization parameter, computational methods in medical imaging.

# Publications

1. Ravi Prasad K. Jagannath and Phaneendra K. Yalavarthy, “*Approximation of Internal Refractive Index Variation Improves Image Guided Diffuse Optical Tomography of Breast*,” IEEE Transactions on Biomedical Engineering **57(10)**, 2560–2563 (2010).
2. Ravi Prasad K. Jagannath and Phaneendra K. Yalavarthy, “*Minimal Residual Method Provides Optimal Regularization Parameter for Diffuse Optical Tomography*,” Journal of Biomedical Optics **17(10)**, 106015:1–7 (2012).
3. Ravi Prasad K. Jagannath and Phaneendra K. Yalavarthy, “*An Efficient Gradient-Free Simplex Method for Image-Guided Diffuse Optical Tomography*,” Journal of Biomedical Optics **18(4)**, 030503:1–3 (2013).
4. Ravi Prasad K. Jagannath and Phaneendra K. Yalavarthy, “*Non-quadratic Penalization Improves Near Infrared Diffuse Optical Tomography*,” Journal of the Optical Society of America A: Optics, Imaging Science, and Vision **30(8)**, 1516–1523 (2013).

# Contents

<b>Acknowledgements</b>	i
<b>Abstract</b>	ii
<b>Keywords</b>	v
<b>Publications</b>	vi
<b>1 Introduction</b>	1
1.1 Traditional Breast Imaging Techniques . . . . .	1
1.1.1 X-ray Mammography . . . . .	2
1.1.2 Magnetic Resonance Imaging (MRI) . . . . .	3
1.1.3 Ultrasound . . . . .	4
1.2 Diffuse Optical Tomographic Imaging of breast . . . . .	5
1.2.1 Forward Problem . . . . .	8
1.2.2 Inverse Problem . . . . .	10
1.3 Multi-Modal Diffuse Optical Tomography . . . . .	16
1.3.1 <i>Soft-Priors</i> . . . . .	17
1.3.2 <i>Hard-Priors</i> . . . . .	19
1.4 Contribution of the Thesis . . . . .	20
1.5 Organization of the Thesis . . . . .	23
<b>2 MRM-based Optimal Regularization Parameter</b>	25
2.1 Introduction . . . . .	25

2.2	Regularization Parameter for Inverse problem . . . . .	26
2.2.1	Existence of Optimal Regularization Parameter . . . . .	28
2.2.2	Regularized Minimal Residual Method . . . . .	30
2.2.3	Estimating Optimal Regularization Parameter using Minimal Residual Method . . . . .	31
2.2.4	Estimating Optimal Regularization Parameter using Generalized Cross-Validation . . . . .	32
2.3	Experimental Studies . . . . .	34
2.3.1	Numerical Experiments . . . . .	34
2.3.2	Gelatin Phantom Experiment . . . . .	35
2.4	Comparison of Image Reconstruction Results . . . . .	40
2.5	Discussion . . . . .	41
<b>3</b>	<b>Non-Quadratic Penalization in DOT</b>	<b>43</b>
3.1	Introduction . . . . .	43
3.2	Non-Quadratic Penalization : Framework . . . . .	44
3.2.1	Optimal Regularization Parameter using GCV . . . . .	47
3.3	Experimental Studies . . . . .	48
3.3.1	Numerical Experiments . . . . .	48
3.3.2	Gelatin Phantom Experiment . . . . .	49
3.3.3	Quantitative Analysis . . . . .	49
3.4	Results . . . . .	54
3.5	Discussion . . . . .	56
<b>4</b>	<b>Refractive Index Variation in IG-DOT</b>	<b>58</b>
4.1	Introduction . . . . .	58
4.1.1	Estimation of Jacobian . . . . .	61
4.1.2	Simulation studies using realistic 3D breast models . . . . .	62
4.2	Discussion . . . . .	65

<b>5 Gradient-Free Simplex Method for IG-DOT</b>	<b>68</b>
5.1 Introduction . . . . .	68
5.2 Gradient-Free Simplex Method . . . . .	69
5.2.1 Nelder and Mead simplex algorithm . . . . .	69
5.3 Simulation Studies . . . . .	72
5.4 Gelatin Phantom Study . . . . .	73
<b>6 Conclusion</b>	<b>76</b>
<b>A List of Packages/Programs</b>	<b>79</b>
A.1 Packages . . . . .	79
A.2 Developed Programs . . . . .	80
<b>References</b>	<b>82</b>

# List of Figures

1.1	Spectra of the principal absorbers of near-infrared light in tissue [17]. . . . .	6
1.2	The Forward and Inverse Problem in Diffuse Optical Tomography: An illustration [41, 42]. . . . .	8
1.3	Image reconstruction procedure followed in Diffuse Optical Tomography: Flow chart. . . . .	14
2.1	The semi-logy plot of the objective function ( $\Omega =   y - G(\mu_a^\alpha)  _2^2$ ) versus regularization parameter $\alpha$ for the results presented in Fig. 2.5 (first iteration of the 1% noisy data case). The optimal $\alpha$ , indicated by $\alpha^*$ in the plot, is where $\Omega$ takes the minimal value. . . . .	28
2.2	Reconstructed $\mu_a$ distributions using Standard (direct inversion) and Minimal Residual Methods (iterative inversion) with numerically generated 1% noisy data and $\alpha$ being 0.01. One-dimensional cross-sectional plot of $\mu_a$ along the line (shown on the target) for the target and reconstructed results presented here are given in the second row. . . . .	33
2.3	Gelatin phantom used in the experimental studies [42, 43, 60]. . . . .	35
2.4	Plot of the estimated regularization parameter ( $\alpha$ ) using MRM and the corresponding data-model misfit ( $\Omega =   y - G(\mu_a)  _2^2$ ) as a function of the inner iteration number for the first global iteration of the results presented in Fig. 2.5. . . . .	36

2.5	Comparison of reconstruction performance using the two methods discussed in this work for the two circular targets of dimension 7.5 mm radius separated by a distance of 5mm with numerically generated 1% and 3% noisy data. The reconstructed images obtained along with corresponding method with the percentage of the noise added (given on top of image) are given along with the target image. One-dimensional cross-sectional plot of $\mu_a$ along the line (shown on the target) for the target and reconstructed results presented here are given in the second row. . . . .	37
2.6	Similar effort as Fig. 2.5 with the anomalies placed in an asymmetric position for the case of simulation data with 1% noise. . . . .	38
2.7	Similar effort as Fig. 2.5 with the three anomalies placed in the position as shown in the figure labeled as ‘target’ with 1% noise added to data. .	38
2.8	Similar effort as Fig. 2.5 for the case of experimental gelatin phantom data.	39
3.1	Reconstructed images using the penalization functions discussed in this chapter in the numerical experiment with 1% noisy data involving the target distribution given on top-left corner of the figure. The penalization functions are given correspondingly on top of each reconstructed image. The one-dimensional cross-sectional profile along the solid line of the target distribution is given on the top-right corner. . . . .	51
3.2	Similar effort as in the Fig. 3.1. except data noise level being 3%, the target distribution is same as Fig. 3.1. . . . .	51
3.3	Similar effort to Fig. 3.1 except the target is located at the centre having contrast of 4:1. . . . .	52
3.4	Similar effort to Fig. 3.1 except the target is L-shaped. . . . .	52
3.5	Reconstructed optical images with various penalty functions listed in Table-3.1 using realistic MRI derived patient mesh. The one-dimensional cross-sectional profile along the sold line of target distribution is given on the top-right corner. . . . .	53

3.6	Reconstruction results obtained using multi-layered gelatin phantom experimental data. . . . .	53
4.1	Reconstructed distributions of $\mu_a$ (top row) and $\mu'_s$ (bottom row) using the three strategies discussed in Sec. 4.2.2. (given on top of each column) along with the target distributions (first column) for 1915 mesh. The source/detector fibers are indicated by filled circles in the $\mu_a$ distribution of the target. The estimated optical properties for this 1915 mesh are also listed in Table 4.1. . . . .	67
5.1	Comparison of reconstruction performance for the case of numerically generated data with 1% noise. The reconstruction techniques that were used are given on top of each figure, with the traditional being LM method, Proposed being the Nelder-Mead simplex method, and target represents actual $\mu_a$ distribution. The initial guess for the top row is $0.01 \text{ mm}^{-1}$ and for the bottom row it is $0.001 \text{ mm}^{-1}$ . . . . .	70
5.2	The one-dimensional cross-section plot along the dotted line on the target image (given at the top left corner of the Fig. 5.1) for all the reconstruction results shown in Fig. 5.1. . . . .	71
5.3	Similar effort as in Fig. 5.1 for the case of experimental gelatin phantom data. The initial guess here is obtained using the data-calibration procedure.	74

# List of Tables

2.1	Comparison of total computational time (in seconds) including the overhead, for three reconstruction results (first column) presented in the Fig. 2.5 for the 1% noise case. The corresponding method is given in the first row of the table. The total number of iterations taken to converge are given in the parenthesis. . . . .	37
3.1	Different penalty functions and their derivatives that are deployed for estimation of optical properties using Eq. 3.4 . . . . .	45
3.2	Quantitative comparison of relative error ( $RE$ , Eq. 3.9) of the reconstruction results using the penalty functions discussed in this chapter. . . . .	55
3.3	Quantitative comparison of Pearson correlation ( $PC$ , Eq. 3.10) of the reconstruction results using the penalty functions discussed in this chapter.	56
4.1	Estimated optical properties (in $\text{mm}^{-1}$ ) of each region using the three strategies discussed in Sec. 4.2.2 for six meshes. . . . .	64
4.2	Estimated optical properties (in $\text{mm}^{-1}$ ) of each region of 1915 mesh using three fiber layers with RI-U strategy for $RI = 1.467, 1.4$ . and $1.33$ . The target values are given in the second row of Table 4.1. . . . .	64

# Chapter 1

## Introduction

Molecular imaging using optics has seen tremendous growth in the last decade, including development of advanced numerical and mathematical models that can make these imaging modalities more quantitative in nature. These optical molecular imaging modalities have been imaging mainly breast and brain tissues *in-vivo*. Breast cancer has the second largest cancer mortality percentage in the United States [1]. An estimated 226,870 new cases of breast cancer are expected to occur among women in the US during 2012 [1]. Early diagnosis and proper detection play a very important role in treating cancerous tissues and the same is achieved by advanced optical molecular imaging systems. The following sections briefly discusses the current trends in clinical breast imaging, to allow the interpretation of optical imaging in the appropriate context.

### 1.1 Traditional Breast Imaging Techniques

In the medical imaging techniques used in radiology, the energy used to produce the image must be capable of penetrating several layers of tissues. Visible light has limited ability to penetrate and is not a preferred choice for medical imaging but used elsewhere like dermatology (skin photography) and pathology (light microscopy) [2] which uses thin sections ( $mm$ ) of tissue. In diagnostic radiology, the electromagnetic radiation outside the visible light region is used for X-Ray imaging, including mammography and

computed tomography (CT), magnetic resonance imaging (MRI), and nuclear medicine. In the form of high-frequency sound waves, is used in ultrasound imaging [2]. The different modes which use different parts of Electro-magnetic (EM) energy spectrum for developing images are referred to as *modalities*. Each of these modalities has its own applications in medicine. The following sections discuss the traditional breast tissue imaging modalities.

### 1.1.1 X-ray Mammography

X-rays are the oldest and most frequently used electromagnetic radiation for medical imaging. X-ray images are the maps of x-ray attenuation coefficient of the tissue under investigation, and hence provides mainly morphological information. X-ray energies between  $\sim 15\text{KeV}$ – $30\text{ KeV}$  are used to examine breasts and is clinically used for screening the breasts for early detection and diagnosis of women with breast symptoms such as the presence of a lump (diagnostic mammography) [2]. Sensitivity is evaluated by dividing the number of positive breast cancer cases detected by the total sum of those that were detected plus those that were missed. In this context, sensitivity may also be defined as the likelihood of identifying a positive case when presented with one. Estimates of the sensitivity of screening mammography from different studies range from 83 to 95 percent [3–5]. Specificity refers to the proportion of true-negative results, or tests that correctly indicate that a woman does not have breast cancer among screened women without breast cancer. Mammography specificities generally fall in the range of 90 to 98 percent. In other words, the worst risk of a false-positive mammogram is about 1 in 10. [6,7]. This means a large fraction of the suspicious structures identified in mammograms are not cancerous and must be followed by surgical biopsies. The additional limitation of X-ray mammography is that its sensitivity for cancer is significantly decreased with glandular and radio-graphically dense breasts. The fact that X-rays use ionizing radiation for imaging, there are concerns in the dose used in this imaging, and many routine screenings in younger women is not supported due to the dose constraints. Another important issue is the diagnosis of ductal carcinoma in situ (DCIS) is not possible with

mammography [4, 6, 7]. As mammography is the radiography of the breast it is largely an anatomical imaging modality whose detection is based upon architectural distortions and micro-calcifications within the breast, this information provides tissue functional information for the diagnosis of the breast cancer [4]. This allows imaging modalities that provide a different and complimentary set of information (Optical imaging) apart from architectural distortion to be combined with mammography.

### 1.1.2 Magnetic Resonance Imaging (MRI)

Magnetic Resonance Imaging is the most significant development in medical diagnosis since the discovery of the x-ray. Strong magnetic fields that are about 10,000 to 60,000 times stronger than the earth's magnetic field [2] are used in MR scanners. Most MR scanning protocols utilize the nuclear magnetic resonance properties of the proton i.e., the nucleus of the hydrogen atom ( $H^+$ ) which is found in abundance in biological tissues. When this atom is placed in a 1.5 tesla ( $T$ ) magnetic field, the proton will preferentially absorb radio wave energy at the resonance frequency of  $63MHz$ . The absorbed radio waves are subsequently remitted from the patient after a period of time that depends on the local magnetic properties of the tissue. The MRI systems use the frequency and phase of the returning radio waves to determine the position of each signal from the patient. MRI gives a set of tomographic slices of the patient depicting the micro-magnetic properties of the the tissue with very high soft-tissue contrast. Another reason for MRI being considered as effective imaging modality in the past few decades is because it uses non-ionizing radiation, especially in cases of complex tissues or where the patient is prone to a higher risk of breast cancer. Detection of the presence of motion is possible in contrast-enhanced MRI which is used for blood flow monitoring, in which injection of gadolinium based agents are used as contrast enhancers. Contrast-enhanced breast MRI has very good sensitivity (98%) and low specificity (64%) [8, 9]. High cost involved and long scan times are main drawbacks attributed to the MR imaging. In theory, MR spectroscopy is capable of revealing the functional properties of the tissue (e.g. water, fat content), accurate diagnosis of breast cancer is still an active research area [9].

MRI is capable of providing the paramagnetic deoxygenated hemoglobin content, but it is an indirect way of quantifying the oxygenated hemoglobin, making the oxygen saturation measurements more error prone [10]. The oxygen saturation assesses the tissue patho-physiological state. Hence there is room for imaging modalities to add functional information to the structural information, and in this thesis we will examine this in the context of hybrid imaging modalities.

### 1.1.3 Ultrasound

Ultrasound machinery tries to image the internal structures of the biological tissues by transmitting focused beams of sound waves of high- frequency (1 to 10 million cycles per second) and then listening for the reflected sound waves that arise from changes in acoustic impedance as sound waves travel from one tissue type to another. Normally, a short-duration pulse of sound is generated by an ultrasound *transducer* that is in direct physical contact with the tissue-surface that is being imaged and the sound waves travel into the tissue, and are reflected by internal structures in the body, creating echoes. The same transducers record the returning sound stream, the echoes from each line are recorded and used to form an ultrasonic image [2]. Since ultrasound can distinguish subtle variation among soft tissues, fluid-filled tissues cysts, it is particularly useful in imaging the abdomen. Like MRI, ultrasonography does not expose a patient to ionizing radiation a factor that is particularly important for pregnant patients and young patients, and it is being used for routine examination of breast when mammography does not provide good discrimination of the tissue features. Typical values of sensitivity and specificity reported in the literature are 97% and 85% respectively [11], and of course these values are highly dependent on the technician proficiency. One of the drawbacks of ultrasound is is ineffectiveness in visualization of deeper lesions, making it not highly desirable for deep-tissue imaging, especially in large breasts.

## 1.2 Diffuse Optical Tomographic Imaging of breast

Over the last few decades, the field of biomedical optics has emerged with novel technologies to extract clinically relevant structural and functional information from biological tissues, non-invasively. Many of these techniques, such as diffuse optical imaging, make use of the optical absorption characteristics of the tissue chromophores, like hemoglobin, allowing the measurement of tissue oxygenation, blood flow and oxygen metabolism. The non-invasive, portable and low cost benefits of optical techniques made them employable across the range of clinical and life sciences. For example, there is now widespread application in human brain mapping, in vivo gene expression studies in biology and medicine, the clinical assessment of a range of neurological conditions and the monitoring of muscle physiology and pathophysiology [12–14].

The development of complex theoretical models of light transport in tissue, which have guided instrument design and allowed reconstruction of three-dimensional optical images. In particular, optical imaging is a rapidly emerging field, with applications ranging from clinical diagnosis to molecular biology. Optical imaging techniques have considerably impacted the treatment and/or prevention of cancer and of other lethal diseases [15, 16]. This is mainly because of the following reasons: (a) can probe both functional and structural changes in the tissue; (b) are non-invasive and non-ionizing; (c) can be portable and of low equipment cost; (d) provide results almost in real time; (e) can provide quantitative information for objective diagnosis and follow-up.

Diffuse optical tomographic imaging is a non-invasive medical imaging method applied to quantitatively estimate the optical properties of soft tissues. Near Infrared (NIR) light is used as probing media as it is passed through the tissue and collected on the boundary from which internal distribution of the optical properties are estimated. In the near-infrared (NIR) spectral window of 600-1000 nm, light propagation in tissues is dominated by light scattering rather than absorption. Photons experiencing multiple

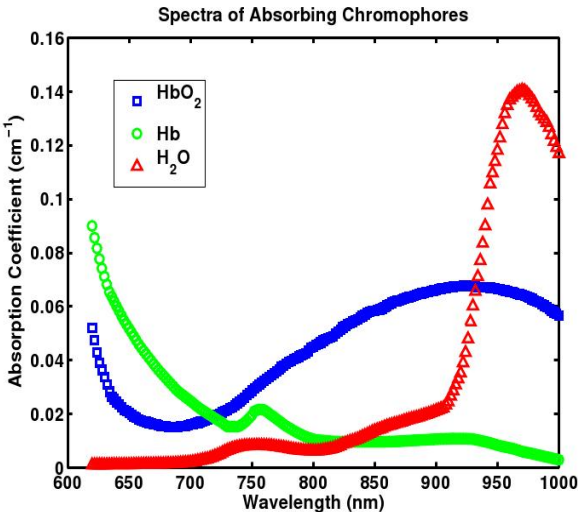


Figure 1.1: Spectra of the principal absorbers of near-infrared light in tissue [17].

scattering events can propagate only limited distance into tissue (up to 10 cm). The chromophores in the tissue are oxygenated hemoglobin ( $\text{HbO}_2$ ), deoxygenated hemoglobin (Hb), water ( $\text{H}_2\text{O}$ ) and lipid. As shown in Fig. 1.1, water molecules in the blood do not absorb much of the NIR light up to 600 nm [17]. Even though the absorption of light by water is very low at lower wavelengths but dramatically increases at higher wavelengths. As a result, there is a window in the NIR from about 650-950 nm where light can penetrate more deeply into the tissue and can give appreciable level boundary measurements. A weighted sum of the contributions from each chromophore corresponds approximately to bulk optical absorption coefficient ( $\mu_a$ ) of the tissue [17].

One of the main obstacle for the propagation of NIR light is the high degree of light scattering that occurs, which limits the use of existing techniques to a few millimeters. The mean free path of visible light in tissue is only about  $100 \mu\text{m}$ , and multiple scattering events will cause the direction of the average photon to be randomized after about 1 mm. However, the problem is not that NIR light cannot penetrate deeply into tissue, it does, for instance, NIR light transmitted through 10 cm of human breast tissue can be

detected [17]. The problem arises beyond a few millimeters deep, almost all of the remaining photons would have been scattered multiple times, and their paths taken would be random. Thus, in order to acquire information about tissues deep below the surface, a method is required which allows this information to be extracted from detected photons which have been scattered many times. Unlike the traditional imaging modalities, X-ray CT, SPECT and PET, diffuse optical tomography (DOT) uses non-ionizing radiation which poses no risk to the patient. It is relatively inexpensive as compared to the MRI scanners. The unique feature of diffuse optical imaging is that it acquires information about tissue that is unique, such as light scattering and hemoglobin concentrations. The initial studies exploring the use of diffuse optical imaging for breast cancer diagnosis have shown potential, but significant work remains to be done if diffuse optical imaging is to be successfully translated to a clinical setting to detect cancers. More effective reconstructed images in terms of qualitative and quantitative nature require new instrumentation and image reconstruction techniques.

Diffuse optical tomography involves solving two problems [40], which are illustrated in Fig. 1.2 where  $\mu_a$  and  $\mu'_s$  represent the optical absorption and reduced scattering coefficients of the tissue and “Fibers” represents the optical fibers with dual function of both delivering light and also collecting the exiting light. The optical absorption  $\mu_a$  is defined as the probability of photon absorption in a medium per unit length and the scattering coefficient  $\mu_s$  is defined as the probability of photon scattering in a medium per unit path length. The reduce scattering coefficient  $\mu'_s$  is, by definition,  $\mu'_s = \mu_s(1-g)$ , where  $g$  represents the anisotropic scattering factor of the medium. The forward problem is solved to calculate the boundary data ( $y$ ), for a given set of optical distribution ( $\mu_a$  and  $\mu'_s$ ) in the tissue, using a model for light transport in tissue. While solving the inverse problem involves reconstructing the optical distribution ( $\mu_a$  and  $\mu'_s$ ) given the limited boundary data ( $y$ ) using an iterative scheme because of the non-linear nature of the problem. The subsequent sections will discuss these two problems in length.

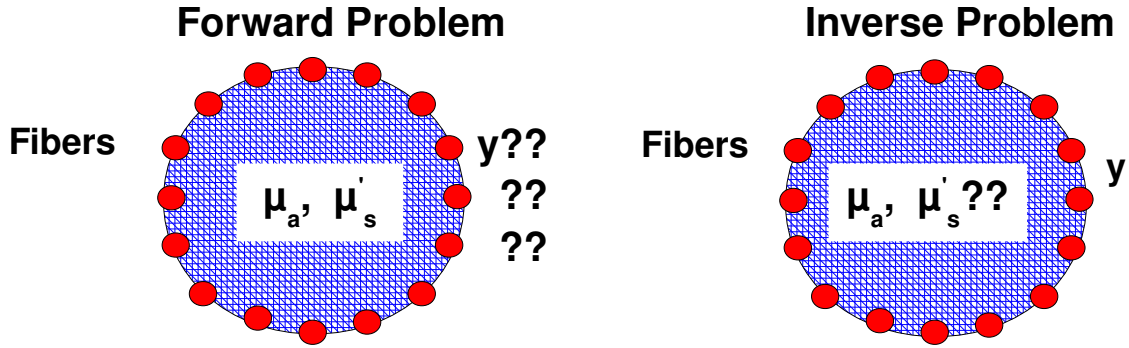


Figure 1.2: The Forward and Inverse Problem in Diffuse Optical Tomography: An illustration [41, 42].

### 1.2.1 Forward Problem

Near Infrared (NIR) light propagation, in regime of turbid media such as tissue, is erratic moving photons with large interactions and migrating on average through the medium like a propagating wave [18, 24]. Accurate computational model for the propagation of light in diffusive tissue is achieved by the steady-state Diffusion Equation (DE), which is an approximation to the Radiative Transport Equation (RTE). In the frequency-domain, the DE is given by [18, 22–24]

$$-\nabla \cdot [D(r)\nabla\Phi(r, \omega)] + \left[\mu_a(r) + \frac{i\omega}{c}\right]\Phi(r, \omega) = Q_o(r, \omega) \quad (1.1)$$

where the optical diffusion and absorption coefficients are given by  $D(r)$  and  $\mu_a(r)$ , respectively. Note that,

$$D(r) = \frac{1}{3[\mu_a(r) + \mu'_s(r)]} \quad (1.2)$$

where  $\mu'_s$  is the reduced scattering coefficient, which is defined as  $\mu'_s = \mu_s(1 - g)$ .  $\mu_s$  is the scattering coefficient and  $g$  is the anisotropy factor. The light source is represented by  $Q_o(r, \omega)$  modeled as isotropic placed at one scattering distance inside the domain to be imaged. The photon fluence rate at any given position  $r$  is represented as  $\Phi(r, \omega)$ . The modulation frequency  $\omega$  is defined as  $\omega = 2\pi f$ . Speed of light in tissue ( $c$ ) is given

by,  $c = \frac{c_v}{n}$  with  $c_v$  representing the speed of light in the vacuum and  $n$  is the refractive index of the tissue. The velocity of light  $c_v$  is assumed to be constant throughout the imaging domain ( $\approx 2.86 \times 10^8$  m/sec).

On other hand, continuous wave (CW) instruments use continuously emitting light as the probing signal and just measure the relative attenuation of light through tissue. These instruments are relatively cheap and easy to build compared to their counter parts as the measurements are only the light intensities. In this mode, data acquisition is continuous-wave (intensity alone) data at the boundary of the tissue under investigation [18], and the diffusion equation for the continuous-wave domain is given as,

$$-\nabla \cdot [D(r)\nabla\Phi(r)] + \mu_a(r)\Phi(r) = Q_o(r) \quad (1.3)$$

which has the usual notations as mentioned for diffusion equation in frequency-domain (Eq. 1.1). In this domain  $\mu'_s$  is assumed to be known and remains constant throughout the domain and only the optical parameter  $\mu_a$  is assumed to vary in the imaging domain. Continuous wave measurements are known to be difficult to calibrate to account for coupling errors [24]. Since most of the functional parameters of the tissue can be calculated from absorption coefficient estimation at multiple wavelengths, assuming the scattering constant, could have large clinical applicability for the simplicity of use and low cost. Boundary condition for the diffusion equation (for both Eq. 1.1 and Eq. 1.3), a Robin-type (Type-III) boundary condition [21] is applied to model the refractive-index mismatch at the boundary and is given by,

$$\Phi(\xi, \omega) + 2A\hat{n} \cdot D(\xi)\nabla\Phi(\xi, \omega) = 0 \quad (1.4)$$

where  $\xi$  is a point on the external boundary, and  $A$  depends upon the relative refractive index mismatch between the imaging domain and the air (Ref. [45,49]). There are three types of methods to solve the diffusion equation mentioned above, namely, *Analytical Methods*, *Statistical Methods* and *Numerical Methods*. However, for the work considered

in this thesis a Finite Element Method (FEM), which is one of the most commonly deployed numerical methods for solving forward problem in complex cases like breast with irregular boundaries, is considered to generate the modeled boundary data  $G(\mu)$  for a given distribution of optical properties  $[\mu]$  where  $\mu(r) = [D(r); \mu_a(r)]$ . This is achieved through usage of open-source Near Infrared Fluorescence and Spectral Tomography Software [NIRFAST] [49]. If  $F$  is assumed to be the forward model, which gives the fluence at every point, then the modeled boundary data,  $G(\mu)$ , is obtained by sampling the forward model at the boundary for a given internal spatial distribution of optical properties and source-detector locations [40], given as

$$G(\mu) = S\{F(\mu)\} \quad (1.5)$$

$F$  is non-linear operator of the optical properties  $\mu$ . The data in frequency-domain, and rather than considering the complex data, the signal is converted to real data [23]. Data ( $y$ ) in the form of natural logarithm of the amplitude ( $A$ ) and phase ( $\theta$ ) of the frequency domain signal ( $y = [\ln A; \theta]$ ). Defining  $A$  and  $\theta$  as follows

$$\begin{aligned} A &= \sqrt{[Re(G(\mu))]^2 + [Im(G(\mu))]^2} \\ \theta &= \tan^{-1} \left[ \frac{Im(G(\mu))}{Re(G(\mu))} \right] \end{aligned} \quad (1.6)$$

The boundary data for the continuous-wave mode is the intensity (amplitude) of the measured signal, which is used with an FEM based reconstruction procedure to obtain the internal spatial distributions of  $\mu_a$ . Here also,  $F$  has a non-linear dependence on  $\mu_a$  and the data ( $y$ ) in continuous-wave domain is the natural logarithm of the amplitude ( $A$ ) of the measured signal ( $y = [\ln A]$ ).

### 1.2.2 Inverse Problem

The inverse problem of diffuse optical tomographic imaging involves reconstructing the optical properties from a limited set of boundary data, as shown in Fig. 1.2. This image

reconstruction problem is inherently difficult to solve from a mathematical/computational point of view. This challenge is primarily due to the fact that the transport model itself is non-linear, leading to an inverse problem which is ill-posed. By definition,

- Non-linear : The detected signal is not a linear function of the optical properties.
- Ill-posed : Small errors in the detected signal leads to large changes in estimated optical properties, making this problem prone to large estimation error due to noise in the data.
- Under-determined : also known as ill-determined. Number of independent equations (equivalently, number of independent measurements) are much less than number of unknowns (optical properties).

These characteristics results in the existence of infinite number of solution to the problem for a given set of measurements [22]. This non-uniqueness problem results in a need to constrain the solution space and to bring about stability to the solution by using mathematical methods known as regularization. Regularizing the problem requires formulating the inversion as an iterative model-based linear algebra problem. A detailed discussion of this is presented in this section.

The relation between  $\mu$  and  $F$  is non-linear (as explained earlier Eq. 1.5), in order to solve the inverse problem the forward problem is linearized. Now, if we assume the forward model for a given  $\mu$  distribution and source-detector positions is perfect, then the forward model can be written as,

$$y = G(\mu) \quad (1.7)$$

Now, to estimate the  $\mu$  distribution for the given source and detectors position we have to invert the operator  $G$ , that is,

$$\mu = G^{-1}(y) \quad (1.8)$$

The non-linearity and ill-posedness in the problem makes it impossible to invert this operator in one step. In practice, this inversion is performed by taking series of linear steps. Hence the problem is linearized by assuming the actual properties ( $\mu$ ) are close to the initial estimate  $\mu_0$  and the experimental data ( $y$ ) is close to the modeled data ( $y_0$ ) which can be obtained using a calibration procedure [21]. Expanding Eq. 1.7 around the initial estimate ( $\mu_0$ ) using a Taylor series,

$$y = G(\mu_0) + G'(\mu_0)(\mu - \mu_0) + \dots \quad (1.9)$$

Neglecting the higher-order terms and considering linear term results in,

$$\Delta y \approx \mathbf{J} \Delta \mu \quad (1.10)$$

where  $\Delta \mu = (\mu - \mu_0)$  being the variables of the equations and helps in updating the optical properties,  $\Delta y = (y - y_0)$  called as the data-model misfit,  $y_0 = G(\mu_0)$ , and Jacobian or the sensitivity matrix  $\mathbf{J} = \frac{\partial G(\mu)}{\partial \mu}$ , the  $\mathbf{J}$  is of size  $2NM \times 2NN$ , where  $NN$  is the number of finite element (FEM) nodes and  $NM$  represents the number of measurements. The Jacobian ( $\mathbf{J}$ ) can be calculated using the perturbation approach, as it is computationally expensive and other alternative used for the imaging domain is the adjoint method [20] which has a high computational gain compared to the perturbation approach. Note that inverting Eq. 1.10 requires regularization because  $\mathbf{J}$  is ill-conditioned matrix. The following paragraphs discuss the most frequently used methods to solve this inverse problems.

The Least-squares (LS) approach is one common approach to solve the inverse problem where an objective function ( $\Omega$ ) is minimized over the range of optical properties ( $\mu$ ). Methods based on gradient evaluation, requiring less memory space for computation, which does not involve explicit Hessian matrix inversion ( $\mathbf{J}^T \mathbf{J}$  or  $\mathbf{J} \mathbf{J}^T$ ) were also used earlier [25, 26]. But, for a highly non-linear problem such as the one under discussion here, this approach requires an optimization scheme involving inner iteration for choosing the optimal step length in every gradient direction. This leads to many

heuristic line-search methods making the step length determination not being straight forward. The image reconstruction in DOT achieved by applying direct methods, known as full-Newton methods [22, 26]. The LS minimization has the effect of reducing the high frequency noise, leading to smooth images. Probabilistic models [27, 28, 60] were also proposed earlier namely *maximum a posteriori* (MAP) estimation which requires a noise model for both image and data space. The subsequent subsections discuss the mathematical framework of Levenberg-Marquardt (LM) minimization and its variants used, as these methods were extensively deployed in this thesis work.

### Levenberg-Marquardt (LM) Minimization

This approach involves matching the experimental data ( $y$ ) with the modeled data ( $G(\mu)$ ) iteratively in the least-squares sense. The objective function to be minimized is defined as

$$\Omega = \|y - G(\mu)\|_2^2 \quad (1.11)$$

In order to find the minimizer, one sets the first order derivative with respect to  $\mu$  equal to zero, i.e, by satisfying the first-order condition [40] given by,

$$\frac{\partial \Omega}{\partial \mu} = \mathbf{J}^T \delta = 0 \quad (1.12)$$

where  $\delta = y - G(\mu)$ , termed as data-model misfit and with  $\mathbf{J}$  as the Jacobian matrix.

Now, to find the update equation used iteratively is derived by considering the Taylor series on  $G(\mu_i)$  and expanding around the previous estimate  $\mu_{i-1}$  gives,

$$G(\mu_i) = G(\mu_{i-1}) + \mathbf{J} \Delta \mu_i + \dots \quad (1.13)$$

where  $\Delta \mu_i = \mu_i - \mu_{i-1}$ . Now, linearizing the above expansion by ignoring the higher order terms gives,

$$G(\mu_i) \approx G(\mu_{i-1}) + \mathbf{J} \Delta \mu_i \quad (1.14)$$

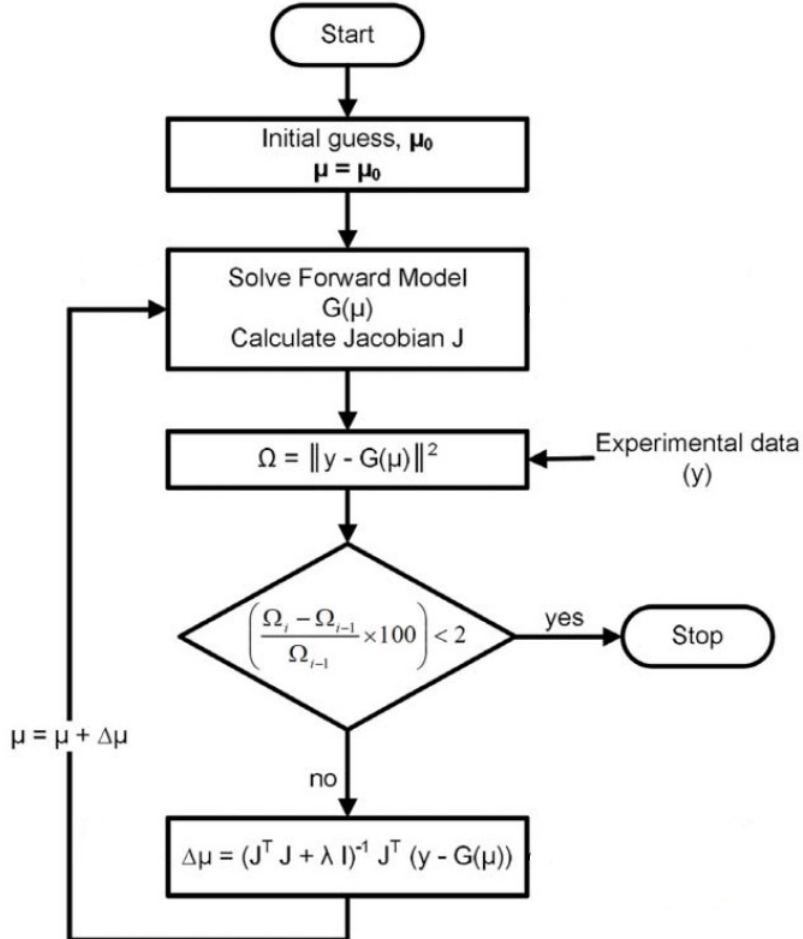


Figure 1.3: Image reconstruction procedure followed in Diffuse Optical Tomography: Flow chart.

Using the above relation in data-model misfit gives,

$$\delta_i = y - G(\mu_i) = y - G(\mu_{i-1}) - \mathbf{J}\Delta\mu_i = \delta_{i-1} - \mathbf{J}\Delta\mu_i \quad (1.15)$$

Generalizing the first order condition (Eq. 1.12) for  $i_{th}$  iteration,

$$\mathbf{J}^T \delta_i = 0 \quad (1.16)$$

Substituting for  $\delta_i$  using the Eq. 1.15 gives,

$$\mathbf{J}^T(\delta_{i-1} - \mathbf{J}\Delta\mu_i) = 0 \quad (1.17)$$

Now, the update equation can be written as,

$$[\mathbf{J}^T\mathbf{J}]\Delta\mu_i = \mathbf{J}^T\delta_{i-1} \quad (1.18)$$

As  $\mathbf{J}^T\mathbf{J}$  is ill-conditioned, a diagonal term is added called as the regularization ( $\alpha$ ) to constrain the solution space,

$$[\mathbf{J}^T\mathbf{J} + \alpha\mathbf{I}]\Delta\mu_i = \mathbf{J}^T\delta_{i-1} \quad (1.19)$$

In LM-minimization,  $\alpha(\geq 0)$  is monotonically decreased with iterations in order to satisfy the first-order condition [29], and with initial condition that  $\alpha \geq \|\delta\|_2^2$ . The advantage of employing this method in here is the simple form of the regularization parameter ( $\alpha$ ), suppressing the high frequency components in the image reconstructed which results in blurring. It is important to realize that the initial estimate ( $\mu_0$ ) has to be close to the actual solution.

In general, the non-linear iterative method of LM minimization is given by

$$\Delta\mu_i = [(\mathbf{J}_{i-1})^T\mathbf{J}_{i-1} + \alpha_i\mathbf{I}]^{-1}(\mathbf{J}_{i-1})^T\delta_{i-1} \quad (1.20)$$

Here,  $\Delta\mu_i$  represents the update of the optical absorption coefficient at the  $i^{th}$  iteration,  $\mathbf{J}^{i-1}$  represents the Jacobian calculated using the optical properties ( $\mu$ ) of the previous iteration ( $i - 1$ ), and  $\alpha(\geq 0)$  is the regularization parameter corresponding to the  $i^{th}$  iteration, and is monotonically decreased with iterations. It typically starts with a number and is reduced by a factor of  $10^{0.25}$  at each iteration [40]. The upper limit on  $\alpha$  is chosen to be a value less than the maximum Eigen value of the  $\mathbf{J}^T\mathbf{J}$  matrix [22], as values greater than this will lead to an over-regularized (smooth) solution. The flow

chart of different steps involved in image reconstruction is shown in the Fig. 1.3. After each inversion the corresponding update in  $\mu_a$  is obtained and corresponding  $\mathbf{J}$  and  $\delta$  are recomputed. The new linear inverse problem is reformulated (Eq. 1.20), this iterative procedure is stopped when the  $\ell_2$  norm of the data-model misfit does not improve by more than 2% [43] which is the typical noise level in the data.

### 1.3 Multi-Modal Diffuse Optical Tomography

Traditional imaging modalities used in the clinic such as CT, MRI, and SPECT/PET can be synergistically combined with the emerging optical imaging modalities like diffuse optical imaging, optical coherence imaging, opto-acoustic imaging. Optical instruments are relatively inexpensive when compared with the traditionally used imaging systems and the other key factor is that multi-modal imaging can simultaneously provide functional information and high-resolution structural details. Since diffuse optical tomography provides patho-physiological information about the tissue there has been a increase interest in research activities to integrate this optical imaging with a traditional imaging modalities, especially for breast cancer imaging. A multi-modality optical imaging example is MRI with near-infrared diffuse optical imaging system that combines the high spatial resolution structural information obtained through MRI with NIR imaging to estimate the optical properties of tissue [30, 31].

The optical imaging has the potential to estimate the concentrations of physiological-state revealing chromophore concentration such as oxygenated- and deoxygenated-hemoglobin by providing absolute spatial quantification of absorption coefficients in the NIR spectrum. Anatomical information derived from a conventional medical imaging modality, like magnetic resonance imaging (MRI) provides structural information at high spatial resolution ( $\sim 1\text{mm}$ ) can be taken into account and be included as *a priori* information during reconstruction to improve the quantitative accuracy of the NIR imaging as it has

relatively poor resolution ( $\sim 4 - 7\text{mm}$ ). Multimodal imaging systems, like MRI combined with NIR imaging [25, 30–39], have the advantage of estimating molecular-specific signatures. Earlier works [22] have also shown that optical contrast obtained through NIR imaging can be correlated to MR contrast and structural MR images can be used to reduce the number of unknown parameters to be estimated to the number of regions identified which is referred to as *hard-priors*. The main difficulty with hard-priors based approach lies in its inability to handle the imperfect *a-priori* information. Carpenter et al [13, 14] performed a study of image-guided spectroscopy on cancerous breast tissue that integrated near-infrared spectroscopy into a MRI breast imaging and showed that their method preserves high resolution and combines the two (NIR and MRI) data sets together. This study also revealed that NIR imaging can eliminate the false-positives detected by MRI in breast cancer imaging. A generalized framework to include priors was proposed by Yalavarthy et al [43] known as the soft-priors, which explores a covariance-based constraint scheme derived from finite differencing of the Helmholtz equation [40], and was shown to allow optical property variation within a given region and also the method reduced biases caused by the use of imperfect prior information. These two main approaches to use the spatial priors namely (1) *Soft-Priors* and (2) *Hard-Priors* are discussed in the next two subsections.

### 1.3.1 *Soft-Priors*

The *soft-priors* based approach to image reconstruction in diffuse optical imaging employs modified the Tikhonov-minimization functional to include the structural information in the regularization term as,

$$\Omega = \min_{\mu} \{ \|y - G(\mu)\|_2^2 + \lambda_i \|\mathbf{L}(\mu - \mu_0)\|_2^2 \} \quad (1.21)$$

where  $\lambda$  is the Tikhonov regularization parameter used to balance the effect of the prior with the data-model mismatch in least-square sense, represented as  $y - G(\mu) = \delta$ , and  $\mathbf{L}$  is a dimensionless regularization matrix and  $\mu_0$  is the prior estimate of the optical

properties. In order to find the minimizer of the above equation, the first-order condition is used [36–40], given as

$$\frac{\partial \Omega}{\partial \mu} = \mathbf{J}^T \delta - \lambda_i \mathbf{L}^T \mathbf{L}(\mu - \mu_0) = 0 \quad (1.22)$$

Numerical scheme for the above equation for the  $i^{th}$  iteration is,

$$\mathbf{J}_{i-1}^T \delta_i - \lambda_i \mathbf{L}^T \mathbf{L}(\mu_i - \mu_0) = 0 \quad (1.23)$$

Now, substituting Eq.1.23 in the above equation for  $\delta_i = \delta_{i-1} - \mathbf{J}_{i-1} \Delta \mu_i$  and  $\mu_i = \mu_{i-1} + \Delta \mu_i$  leads to

$$\mathbf{J}_{i-1}^T (\delta_{i-1} - \mathbf{J}_{i-1} \Delta \mu_i) - \lambda_i \mathbf{L}^T \mathbf{L}(\mu_{i-1} + \Delta \mu_i - \mu_0) = 0 \quad (1.24)$$

With further algebraic simplification, the update equation can be written as

$$[\mathbf{J}_{i-1}^T \mathbf{J}_{i-1} + \lambda_i \mathbf{L}^T \mathbf{L}] \Delta \mu_i = \mathbf{J}_{i-1}^T \delta_{i-1} - \lambda \mathbf{L}^T \mathbf{L}(\mu_{i-1} - \mu_0) \quad (1.25)$$

A popular choice of  $\mathbf{L}$  for including spatial priors is the Laplacian-type structured regularization matrix [43]. This matrix is generated using anatomically-derived priors and effectively relaxes the smoothness constraints at the interface between different tissue layers, in directions which is common to their sharing boundary. Usage of Laplacian-type regularization matrix was shown to be more robust, which could easily encode internal boundary information from anatomical information [43]. The Laplacian ( $\mathbf{L}$ ) matrix contains the region information with entries as 1 on the diagonal,  $\mathbf{L}_{ij} = -1/n$  at the off-diagonal entries when  $i$  and  $j$  belong to the same region containing  $n$  number of nodes, and 0 else where. The term  $\mathbf{L}^T \mathbf{L}$  in the Eq. 1.25 approximates a second order Laplacian smoothing operator within each region separately or in other words it averages the update within a region [43].

### 1.3.2 Hard-Priors

Inclusion of structural information can be achieved through *hard-priors* approach, also known as *Image Guided Diffuse Optical Tomography* (IG-DOT), in which the parameter or image space is constrained to the number of regions segmented from a high resolution anatomical imaging modality [43]. The estimation of optical properties ( $\mu$ ) is achieved through the Levenberg-Marquardt (LM) minimization except that the number of unknowns is now reduced to the distinct tissue types. The update equation used to estimate the unknowns is given in Eq. 1.20 with Jacobian ( $\mathbf{J}$ ) having the size of  $(2NM \times 2NR)$ , where  $NM$  and  $NR$  are the number of measurements and the number of regions respectively. The advantages of using this method is that the problem is no more underdetermined since there are more measurements compared to the number of unknowns and also inverting such a matrix is computationally efficient when compared to the traditional approach in which the Jacobian  $\mathbf{J}$  is of size  $2NM \times 2NN$ , where  $NN$  is the number of finite element (FEM) nodes. The main limitation of *hard-priors*-based approach is that the uncertainty in the anatomical priors may get amplified in the reconstructed image. In order to reduce the number of unknowns, typically a mapper matrix ( $\mathbf{R}$ ) is used i.e.

$$\tilde{\mathbf{J}} = \mathbf{JR} \quad (1.26)$$

Here,  $\mathbf{R}$  has a size of  $2NN \times 2NR$  (being matrix) [43]. In essence, the new Jacobian ( $\tilde{\mathbf{J}}$ ) matrix elements are produced by adding the sensitivity of nodes belonging to the same region. The update equation (Eq. 1.20) uses the reduced Jacobian ( $\tilde{\mathbf{J}}$ ) instead of  $\mathbf{J}$  to estimate the segmented optical coefficients ( $\tilde{\Delta\mu}$ ). It is important to understand that the inversion of the Hessian even in this case is still ill-posed and requires regularization. Once the update equation is solved, in order to obtain the original solution vector of dimension  $2NN \times 1$ , the following transformation is required [43]

$$\Delta\mu = \mathbf{R}\tilde{\Delta\mu} \quad (1.27)$$

This approach still used the LM-minimization scheme, which utilizes regularization parameter (Eq. 1.20).

## 1.4 Contribution of the Thesis

Diffuse optical tomography (DOT) is a functional imaging modality for diagnosis or monitoring of breast tissue and blood oxygenation levels. Due to the multiple scattering, the inherent non-linearity of near infrared (NIR) light propagation in tissues makes computational modeling very challenging task to get solutions accurately, and the inverse problem has infinitely many solutions for the given set of boundary data arising out of one physiological condition. Developing computationally inexpensive, robust and novel reconstruction methods is the one of the major challenges in making diffuse optical imaging an effective clinical imaging modality.

Reconstructing the internal distribution of optical properties by solving the inverse problem using the limited boundary data is a challenging task and in general only approximate solutions are obtained. This inverse problem is non-linear, ill-posed and under-determined, which is the result of the multiple scatterings of the light in a dense biological tissue and requires advanced numerical methods to solve it. One of the most powerful methods in existence is the Newton-Raphson based technique via Tikhonov regularization. This involves the inversion of the large Hessian matrix obtained by using the Jacobian (or sensitivity) matrix. This inversion typically requires regularization and most often used one is Tikhonov type regularization. The Tikhonov-type regularization adds a fixed diagonal value to the Hessian, also known as regularization parameter. The regularization parameter in this case dictates the quality of reconstructed image, higher than the optimal value smoothens the reconstructed images resulting in loss of resolution, lower case resulting in high frequency noise in images. This makes the choice of such regularization parameter critical in the image reconstruction procedure. The regularization parameter choice theoretically depends on the noise characteristics both in

data and image space and is highly impractical to obtain the same in real-time leading to empirical choice of the same.

Determination of regularization parameter empirically leads to subjectivity and an unwarranted bias in the solution. One of the most commonly used automated technique for determining the regularization parameter in Newton-type inversion schemes is Generalized cross-validation (GCV), which is often used for Tikhonov type regularization. The GCV method is applicable to linear inverse problems and is widely used in image deblurring. As the inverse problem here is non-linear, which is solved in series of linear steps, application of GCV to find optimal regularization parameter will be shown to be suboptimal for the problem under consideration. More importantly, it will be shown that one can obtain optimal regularization parameter in these cases using the regularized minimal residual method. Such determination of regularization parameter requires an additional optimization procedure and is not computationally expensive compared to the estimation of optical properties. The cases considered here are both numerical as well as gelatin phantom experiments to prove that the proposed minimal residual method provides an optimal regularization parameter.

The regularization term, also known as penalty, choice can influence the image characteristics observed in the reconstructed image. As pointed earlier, Tikhonov-type penalty, which is quadratic, is the most popular among them. A new framework that can easily incorporate these penalty terms is developed, mainly to include non-traditional penalty terms and to effectively assess the improvement in the reconstructed image characteristics. These include,  $\ell_1$ , Cauchy, Geman–McClure and a systematic comparison with the quadratic ( $\ell_2$ ) regularization is performed as a part of this work. The results obtained using numerical and gelatin phantom data indicate that the non-quadratic penalty terms are capable of improving the reconstructed image characteristics in diffuse optical tomographic imaging.

The high-resolution images from traditional imaging modalities, in image guided diffuse optical tomographic imaging, are used to obtain the finite element meshes with segmented regions. Typically the diffusion equation (DE), which is valid for thick tissues, often solved on these meshes using finite element method (FEM). Even though refractive index (RI) of each segmented region is known to be different, a uniform RI is typically used in solving the DE leading to inaccurate modeling of NIR light propagation in tissue. This uniform modeling of RI is primarily due to the fact that the RI for the segmented regions is often not known, especially in *in-vivo*. Moreover, finding the RI distribution for the tissue under investigation should be posed as a new reconstruction problem, which is not so straight forward in the case of unknown optical properties. Earlier investigations in breast imaging [25, 33–38], limited to two-dimensions (also not in the context of IG-DOT), have shown that the uniform modeling of RI will have minimal effect on the estimated optical properties. In here, it was shown that the approximation of internal RI values for the segmented regions (obtained from the literature) in IG-DOT will lead to improved estimates of optical properties.

The *hard-priors* approach makes the diffuse optical image reconstruction problem less ill-posed compared to traditional approach (including *soft-priors*), due to the number of optical parameters to be reconstructed are far lesser compared to the number of measurements available. Specifically, this converts the problem from under-determined in nature to over-determined. Even then the reconstruction procedures that are adapted in the *hard-priors* case are same as the ones used in the traditional approach with most popular one being *Levenberg-Marquardt* (LM) minimization scheme. This LM scheme requires regularization parameter, which not only controls the convergence (number of iterations required), some times leads to biased solutions. Moreover, the LM scheme that is typically adapted to diffuse optical imaging requires calculation of Jacobian (first-order derivative of the model), which is the most computationally expensive step of the image reconstruction procedure. A technique that is a gradient-free simplex method, which does not require regularization as well as computation of gradient (or its variant Jacobian), is

efficient compared to the existing methods for solving the image reconstruction problem in *hard-priors* approach is possible and is proposed in this thesis. The reconstruction results using the proposed method have been compared with traditional methods using numerical and also gelatin phantom experimental cases.

Over all, the main contributions of thesis includes development of novel diffuse optical imaging algorithms that can effectively estimate the optical properties and use the priori/additional information available.

## 1.5 Organization of the Thesis

The thesis is divided into six chapters and the outline of each chapter is as follows. *Chapter-1* gave an introduction to traditional imaging modalities, including optical imaging, followed by a brief introduction to diffuse optical tomography along with multimodal DOT imaging. The reconstruction technique based on Levenberg-Marquardt minimization scheme and image reconstruction methods incorporating spatial priors are also explained.

*Chapter-2* introduces an automated method for optimal selection of regularization parameter that is based on regularized minimal residual method (MRM) is explained and is compared with the traditional generalized cross-validation (GCV) method. As the inverse problem here is nonlinear, application of GCV to find the optimal regularization parameter is known to be suboptimal for the problem under consideration. The results obtained indicate that the MRM-based method is capable of providing the optimal regularization parameter.

*Chapter-3* mainly deals with non-quadratic penalties. The regularization term, also known as penalty, choice can influence the image characteristics observed in the reconstructed image. As pointed earlier, Tikhonov-type penalty, which is quadratic, is

the most popular among them. A new framework that can easily incorporate different penalty terms is developed, mainly to include non-traditional penalty terms including  $\ell_1$ , Cauchy, Geman-McClure and to effectively assess the improvement in the reconstructed image characteristics a systematic comparison with the quadratic regularization is reported in this chapter.

In *Chapter-4*, effect of refractive index in estimating optical properties in IG-DOT is explained using realistic patient 3-D breast meshes. It is shown that by assuming identical refractive index for different regions in breast could lead to erroneous estimation of optical properties. The a priori knowledge of RI should lead to accurate estimation of optical properties. More importantly, in cases where it is not feasible to obtain the RI of different regions of breast, using even approximate values of RI for each region of breast could lead to better estimates of optical properties in IG-DOT.

An efficient gradient-free simplex method for estimation of optical absorption properties in Image-Guided Diffuse Optical Tomography for *hard-priors* approach is analyzed in *Chapter-5* and is shown to be providing solutions that are closely matching with ones obtained using established methods even in highly noisy data case. The explained method also has the distinctive advantage of being more efficient due to being regularization free, involving only repeated forward calculations.

Finally, *chapter-6* brings out the advantages and limitations of the proposed methods in this thesis work and summarizes the research work done and outlines the future work.

# Chapter 2

## MRM-based Optimal Regularization Parameter

### 2.1 Introduction

One of the most powerful methods in existence for solving the inverse problem in diffuse optical tomographic imaging is the Newton-Raphson based technique via Tikhonov regularization [19, 22, 37, 43, 45–51]. This involves the inversion of the large Hessian matrix obtained by using the Jacobian (or sensitivity) matrix. This inversion typically requires regularization and most often used one is Tikhonov type regularization. The Tikhonov-type regularization adds a fixed diagonal value to the Hessian, also known as regularization parameter. The regularization parameter in this case dictates the quality of reconstructed image, higher than the optimal value smoothens the reconstructed images resulting in loss of resolution, lower case resulting in high frequency noise in images. This makes the choice of such regularization parameter critical in the image reconstruction procedure [40, 51, 52]. The regularization parameter choice theoretically depends on the noise characteristics both in data and image space and is highly impractical to obtain the same in real-time leading to empirical choice of the same [40, 51].

Determination of regularization parameter empirically leads to subjectivity and an

unwarranted bias in the solution. Also, such empirical determination varies with the problem at hand and requires prior knowledge about the target images as well as noise in the data. One of the most commonly used automated technique for determining the regularization parameter in Newton-type inversion schemes is Generalized cross-validation (GCV) [53, 54, 58], which is often used for Tikhonov type regularization. The GCV method is applicable to linear inverse problems and is widely used in image deblurring [53, 54, 58, 59]. As the inverse problem here is non-linear, which is solved in series of linear steps, application of GCV to find optimal regularization parameter will be shown to be suboptimal for the problem under consideration. More importantly, it will be shown that one can obtain optimal regularization parameter in these cases using the regularized minimal residual method [60]. Such determination of regularization parameter requires an additional optimization procedure and is not computationally expensive compared to the estimation of optical properties. The cases considered here are both numerical as well as gelatin phantom experiments to prove that the proposed minimal residual method provides an optimal regularization parameter.

As the aim of this chapter is to explain a new way of obtaining the optimal regularization parameter, the discussion is limited to two-dimensional continuous-wave (CW) case, in which the distribution of coefficient of absorption( $\mu_a$ ) is estimated from the limited boundary measurements of the amplitude of exiting light. The implementation of the same is achieved through MATLAB based open-source NIRFAST [50] and the code of the proposed algorithm is also available for enthusiastic users as an open-source [61, 63].

## 2.2 Regularization Parameter for Inverse problem

As stated earlier, the goal of the inverse problem is to recover the distribution of absorption coefficient using the limited number of boundary measurements of light intensity. The inverse problem is typically posed as a least-square minimization scheme [21, 22, 24, 40, 45, 49, 50], where the aim is to iteratively match the modeled data obtained

using the forward problem with the experimentally measured boundary data. A regularization term is typically added to stabilize the solution. The objective function( $\Omega$ ) to be minimized with respect to  $\mu_a$  is written as  $\Omega = ||y - G(\mu_a)||_2^2 + \alpha||\mu_a - \mu_{a0}||_2^2$ . This type of scheme is known to be Tikhonov regularization scheme, where  $y$  is the experimental data collected at the boundary of the object, i.e.  $y = \ln(A)^{measured}$  and  $G(\mu_a)$  is obtained by solving the diffusion-based forward model, as described in the previous section, for the given distribution of the absorption coefficient( $\mu_a$ ).  $\mu_{a0}$  is the initial guess for the absorption coefficient and  $\alpha$  is known to be the regularization parameter. The  $\alpha$  can be shown to be the ratio of variances in the data and estimated properties [43] and such determination requires prior information about the data noise and image noise characteristics, which are difficult to obtain in real-time.

The Taylor series expansion of  $G(\mu_a)$  around the initial distribution of absorption coefficient  $\mu_{a0}$ , as previously explained, gives the objective function as follows

$$\Omega = ||\delta - J\Delta\mu_a||_2^2 + \alpha||\Delta\mu_a||_2^2 \quad (2.1)$$

where  $J = \frac{dG(\mu_a)}{d\mu_a}$  is the Jacobian [64],  $\Delta\mu_a = (\mu_a - \mu_{a0})$  and assuming  $\delta = y - G(\mu_{a0})$  as the data-model misfit. Note that the inverse problem is non-linear and the above equation (Eq. 2.1) is linear, making the non-linear inverse problem to be solved in series of linear steps. The direct solution for Eq. 2.1 is given by [43, 60]

$$(J^T J + \alpha I)\Delta\mu_a = J^T \delta \quad (2.2)$$

which is known to be the Euler equations [60], which is known to be direct method for minimizing the Eq. 2.1. The computational complexity of obtaining a direct solution using the above equation is  $O(NN^3)$ , making it computationally expensive for large problems. After each inversion the corresponding update in  $\mu_a$  is obtained and corresponding  $J$  and  $\delta$  are recomputed. The new linear inverse problem is reformulated (Eq. 2.1), this iterative procedure is stopped when the  $\ell_2$  norm of the data-model misfit does not

improve by more than 2% [43]. Typically  $\alpha$  is chosen empirically at every iteration and is known to influence the reconstructed image quality.

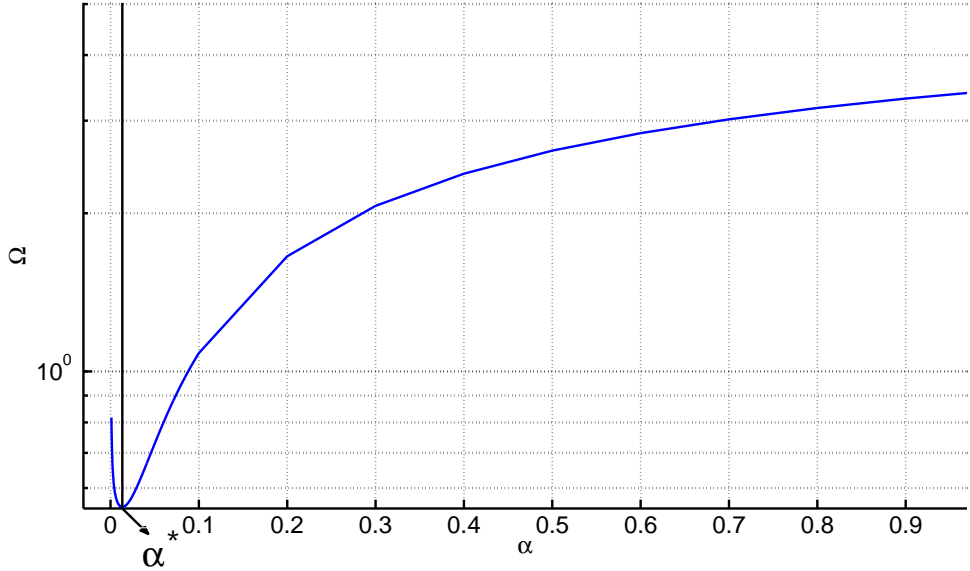


Figure 2.1: The semi-logy plot of the objective function ( $\Omega = \|y - G(\mu_a^\alpha)\|_2^2$ ) versus regularization parameter  $\alpha$  for the results presented in Fig. 2.5 (first iteration of the 1% noisy data case). The optimal  $\alpha$ , indicated by  $\alpha^*$  in the plot, is where  $\Omega$  takes the minimal value.

### 2.2.1 Existence of Optimal Regularization Parameter

In every iterative step of the diffuse optical tomographic image reconstruction the modeled data is matched with the experimental data in the least-square sense. So the objective function to be minimized is posed as follows,

$$\Omega = \|y - G(\mu_a)\|_2^2 \quad (2.3)$$

Since the iterative procedure of minimizing starts with a guess of the initial distribution of the absorption coefficient ( $\mu_{a0}$ ), the above equation Eq. 2.3 can be written as,

$$\Omega = \|y - G(\mu_{a0} + \Delta\mu_a)\|_2^2 \quad (2.4)$$

Applying Taylor's series expansion modifies the above objective function to

$$\Omega = \|(\delta - J\Delta\mu_a)\|_2^2 = (\delta - J\Delta\mu_a)^T(\delta - J\Delta\mu_a) \quad (2.5)$$

The update( $\Delta\mu_a$ ) in the above equation can be obtained using the regularized minimal residual method(MRM) which requires a scalar( $\alpha$ ) as regularization parameter. This implies that for every given positive real number ( $\alpha$ ) there is a unique update ( $\Delta\mu_a^\alpha$ ), in turn making the objective function  $\Omega$  as a continuous function of  $\alpha$ .

Finding the minima of objective function,  $\Omega$ , with respect to  $\alpha$  requires the calculation of first-order derivative, which can be written as

$$\frac{\partial\Omega}{\partial\alpha} = 2 [J^T(J\Delta\mu_a^\alpha - \delta)]^T \left( \frac{\partial\Delta\mu_a^\alpha}{\partial\alpha} \right) \quad (2.6)$$

Similarly, the second-order derivative is given by,

$$\frac{\partial^2\Omega}{\partial\alpha^2} = 2 [J^T(J\Delta\mu_a^\alpha - \delta)]^T \left( \frac{\partial^2\Delta\mu_a^\alpha}{\partial\alpha^2} \right) + \left( J^T J \frac{\partial\Delta\mu_a^\alpha}{\partial\alpha} \right)^T \left( \frac{\partial\Delta\mu_a^\alpha}{\partial\alpha} \right) \quad (2.7)$$

The optimal regularization parameter( $\alpha^*$ ) is the one which makes the first-order derivative (Eq. 2.6) go to zero, simultaneously making the second-order derivative (Eq. 2.7) have a positive value, ensuring that the objective function attains the minimum value.

The optimal solution ( $\Delta\mu_a$ ) for the linearized problem makes the objective function, given by Eq. 2.5, achieve a minimal value. Assuming a perfect system characteristics (including noiseless data), ensures that the residue  $\|r\| = \|(J\Delta\mu_a^{\alpha^*} - \delta)\|$  is zero, where the  $\alpha^*$  represents the optimal regularization parameter. So in the case of  $\alpha^*$ , the right hand side of Eq. 2.6 becomes zero, as  $J\Delta\mu_a^{\alpha^*} - \delta = 0$  (with the partial derivative being non-zero). Using this in the right hand side of Eq. 2.7, results in

$$\frac{\partial^2\Omega}{\partial\alpha^2}\Big|_{\alpha^*} = \left[ \left( \frac{\partial\Delta\mu_a^\alpha}{\partial\alpha} \right)^T J^T J \left( \frac{\partial\Delta\mu_a^\alpha}{\partial\alpha} \right) \right] \Bigg|_{\alpha^*}, \quad (2.8)$$

as  $J^T J$  is symmetric and positive semi-definite matrix [40] and the partial derivative term is non-zero ensures that Eq. 2.8 results in a positive quantity. This assures that  $\alpha^*$  exists for the minimization problem and is achievable when the objective function for the image reconstruction problem has a minima.

This argument could also be validated through graphical representation, by plotting the objective function( $\Omega$ ) as a function of regularization parameter  $\alpha$  for an example problem. Fig. 2.1 shows such an effort for the results presented in Fig. 2.5, where the plot shows  $\alpha^*$  for which the function has a minima, but not zero due to noise in the data and numerical model errors. This makes the choice of  $\alpha^*$  in the real-time (for limited number of iterations) being only sub-optimal (optimal in the asymptotic range).

## 2.2.2 Regularized Minimal Residual Method

The minimization problem that is given in Eq. 2.1 could also be achieved by using the minimal residual method (MRM) [60, 65]. The regularized minimal residual method is equivalent to the regularized steepest descent method and is an iterative technique that minimizes Eq. 2.1. This method could be seen as solving linear system of equation is Eq. 2.1 using an iterative method [60, 65]. The formulation for the  $n^{th}$  update in  $\mu_a$  for a given  $\alpha$  is as follows:

$$(\Delta\mu_a)_{n+1} = (\Delta\mu_a)_n - k_n^\alpha l_n^\alpha \quad (2.9)$$

where,  $l_n^\alpha = J^T r_n + \alpha(\Delta\mu_a)_n$  with  $r_n = J(\Delta\mu_a)_n - \delta$  and

$$k_n^\alpha = \frac{\|l_n^\alpha\|_2^2}{\|Jl_n^\alpha\|_2^2 + \alpha\|l_n^\alpha\|_2^2}. \quad (2.10)$$

The iteration is stopped when the  $\|r_n\|_2^2 - \|r_{n-1}\|_2^2$  is lesser than  $\epsilon = 10^{-6}$  (equal with in single precision limits). The computational complexity of MRM method is  $O(m*NN^2)$ , where  $m$  is the number of iterations needed to reach the stopping criterion. It will be shown later with a numerical example that minimal residual method is equivalent of solving the Euler equation (direct solution) given in Eq. 2.2. This method pseudo-code

is given in Algorithm-1 [42, 60].

---

Reconstruction of  $\mu_a$  corresponding to frame  $n$

INPUT:  $\mathbf{J}|_{\mu_{n-1}}$  and  $\Delta y_n$ ; OUTPUT:  $\Delta \mu_n$ .

Initialize  $\Delta \mu_n^0$  (initial guess),  $\alpha$ .

for  $i = 0, 1, \dots$  (representing inner iteration number)

$$1. \quad r^i = \mathbf{J}|_{\mu_{n-1}} \Delta \mu_n^i - \Delta y_n$$

$$2. \quad l_\alpha^i = l_\alpha(\Delta \mu_n^i) = \{\mathbf{J}|_{\mu_{n-1}}\}^T r^i + \alpha \Delta \mu_n^i$$

$$3. \quad k_\alpha^i = \frac{\|l_\alpha(\Delta \mu_n^i)\|^2}{\|\mathbf{J}|_{\mu_{n-1}} l_\alpha(\Delta \mu_n^i)\|^2 + \alpha \|l_\alpha(\Delta \mu_n^i)\|^2}$$

$$4. \quad \text{Update equation: } \Delta \mu_n^{i+1} = \Delta \mu_n^i - k_\alpha^i l_\alpha^i$$

5. The iterative process, steps: 1-4, is terminated when the misfit reaches the given stopping criterion( $\epsilon_o$ ):  $\|r^i\|^2 \leq \epsilon_o$

---

Algorithm 1: Regularized Minimal Residual (*MinRes*) Method

### 2.2.3 Estimating Optimal Regularization Parameter using Minimal Residual Method

The choice of proper regularization is a key to successful estimation of the optical parameters. The regularization can be obtained optimally using the regularized *MRM*. For every given  $\alpha$  the *MRM* converges to a suitable distribution of the absorption coefficient( $\mu_a$ ) as explained in the previous section. Now this solution of the inverse problem for a given regularization  $\alpha$  can be used to find the corresponding data-model misfit, computed using the updated  $\mu_a$ . This ensures that the data-model misfit ( $\|y - G(\mu_a)\|_2^2$ ), depends only on the scalar quantity( $\alpha$ ). So the optimal  $\alpha$  is the one, which gives the least data-model misfit (or matches the experimental data with the modeled data within a smallest

possible neighborhood). This existence of optimal  $\alpha$  through the proposed method is discussed in the earlier section and shown analytically and graphically that this procedure results in optimal (sub-optimal in noisy data cases) solution for  $\alpha$ . Implementation of finding optimal  $\alpha$  is algorithmically summarized in the following steps.

1. *Compute  $J$ ,  $\mu_a$ , and  $\delta$  for the given iteration .*
2. *Find the  $\alpha$  for which  $\|y - G(\mu_a + \Delta\mu_a^\alpha)\|_2^2$  is minimum, wherein  $\Delta\mu_a^\alpha$  is obtained using regularized MRM described in Sec. 2.2.2 with the inputs computed in step-1.*

For finding such a  $\alpha$ , a gradient-free simplex method type algorithm [66] is used due to its computational efficiency. Note that the objective function in here (Step-2) requires computing the modeled data (or equivalently solving the forward model) at every iteration of finding an optimal  $\alpha$ .

#### 2.2.4 Estimating Optimal Regularization Parameter using Generalized Cross-Validation

The Generalized Cross-Validation(GCV) [53,54,58] method is the most popular method for estimating the regularization parameter( $\alpha$ ). This is based on the principle that an omitted data point could be easily estimated using the regularized solution that is obtained using the reduced data set. Obtaining an estimate of the regularization is achieved by minimizing a function  $G(\alpha)$  defined to be:

$$G(\alpha) = \frac{\|(JJ^T + \alpha I)^{-1}\delta\|_2^2}{(\text{trace}(JJ^T + \alpha I)^{-1})^2} \quad (2.11)$$

Efficient evaluation of the  $G(\alpha)$  is possible by applying the singular value decomposition(SVD) of the Jacobian and doing some algebraic simplification. If the SVD of the Jacobian matrix( $J$ ) is given to be  $J = U\Sigma V^t$ , then the above functional is simplified to the following form,

$$G(\alpha) = \frac{\sum_{i=1}^{\text{rank}(J)} \left( \frac{u_i^T \delta}{\sigma_i^2 + \alpha^2} \right)^2}{\left( \sum_{i=1}^{\text{rank}(J)} \frac{1}{\sigma_i^2 + \alpha^2} \right)^2} \quad (2.12)$$

where the  $i^{th}$  column of the matrix  $U$  is represented as  $u_i$  and  $\sigma_i$  are the singular values of the Jacobian. The function( $G(\alpha)$ ) thus defined is continuous for every value of  $\alpha$  and this is minimized with respect to  $\alpha$  using the same methods as in the previous section and the minimizer thus obtained is the required regularization( $\alpha_{GCV}$ ) for the inverse problem. This is achieved through the usage of MATLAB-based open-source regularization toolbox [59].

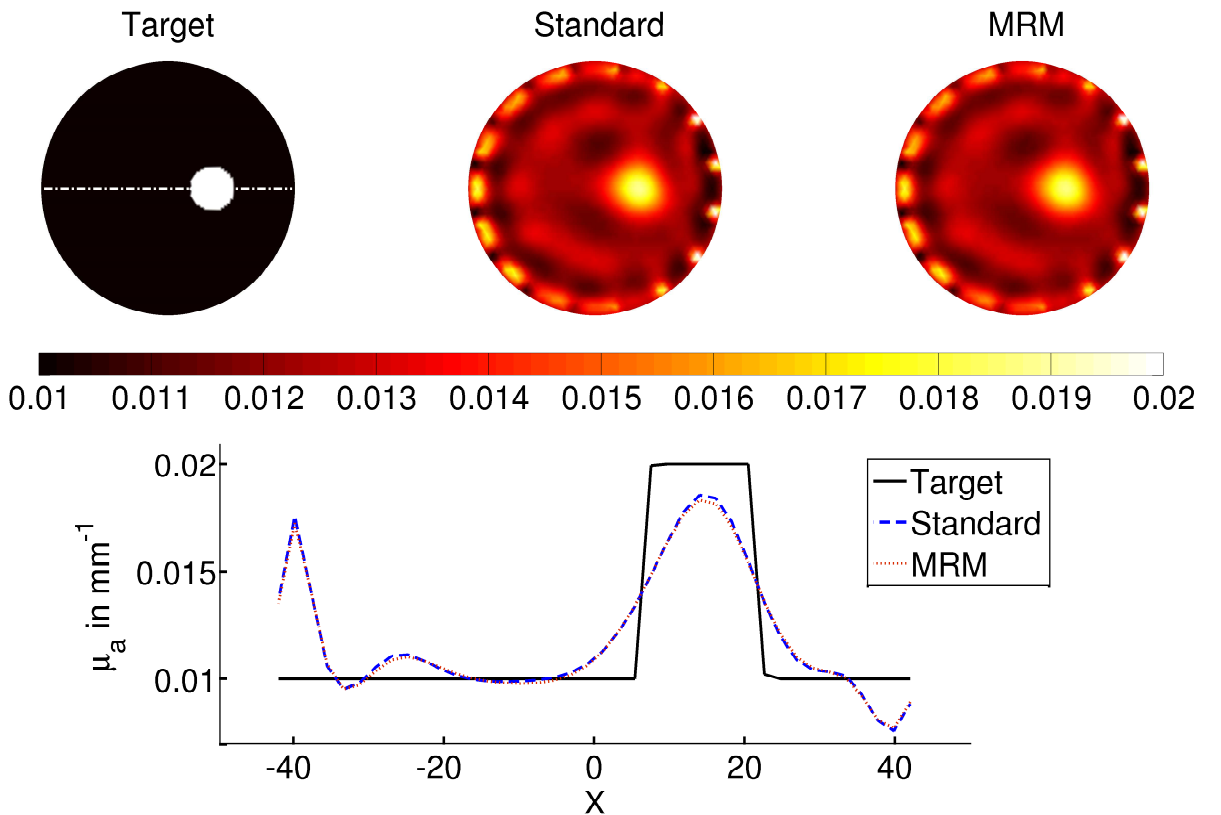


Figure 2.2: Reconstructed  $\mu_a$  distributions using Standard (direct inversion) and Minimal Residual Methods (iterative inversion) with numerically generated 1% noisy data and  $\alpha$  being 0.01. One-dimensional cross-sectional plot of  $\mu_a$  along the line (shown on the target) for the target and reconstructed results presented here are given in the second row.

## 2.3 Experimental Studies

### 2.3.1 Numerical Experiments

The effectiveness of the proposed method is assessed on circular meshes with the background optical properties being [62]  $\mu_a = 0.01 \text{ mm}^{-1}$ ,  $\mu'_s = 1 \text{ mm}^{-1}$  and uniform refractive index of 1.33. The diameter of all the circular meshes used in this work is 86 mm and the experimental data are generated on a fine FEM mesh with 10249 nodes ( $NN$ ) (corresponding to 20160 linear triangular elements) and the reconstruction was performed on a coarser mesh with nodes 1785 ( $NN$ ) (corresponding to 3418 linear triangular elements). The source-detector geometry had 16 fibers that were arranged in circular, equi-spaced fashion and each fibre has a dual function of both acting as source and detector. When one fibre acts as a source the remaining 15 fibers act as detectors and hence we obtain 240 ( $15 \times 16$ ) light amplitude measurements ( $NM$ ). To simulate experimental conditions, the source was modeled as the Gaussian source with a full width at half maximum of 3 mm [55] and was placed at the one mean transport length inside the boundary. All meshes were centered around origin.

The four cases with different targets were considered here, initial case of showing that the solution obtained using MRM is equivalent to standard reconstruction using direct method (Euler equation; Eq. 2.2). For this a circular target of radius 7.5 mm was placed at (15,0) having  $\mu_a = 0.02 \text{ mm}^{-1}$ ,  $\mu'_s = 1 \text{ mm}^{-1}$  and the distribution of  $\mu_a$  is shown in first column of Fig. 2.2. A regularization parameter of 0.01 has been used in this case. A normally distributed Gaussian noise of 1% has been added to the numerically generated data to mimic the experimental case [55]. In the second case, two circular targets that were separated by 5 mm centered around origin with a radius of 7.5 mm were considered. The optical properties were similar to the first case and the target distribution of  $\mu_a$  is given in the first column of Fig. 2.5. In this case, both 1% and 3% normally distributed Gaussian noise added data was considered. In the next case, the two absorbers with 5 mm separation are placed in a position 15 mm away from the centre as shown in Fig. 2.6

and in the fourth case, three absorbers of radius 7.5 mm are placed at the corners of an equilateral triangle of length 16.55 mm as shown in Fig. 2.7. In the previous two cases also, 1% normally distributed Gaussian noise added data was considered to show that effectiveness of the proposed method. At every iteration, the regularization parameter ( $\alpha$ ) has been obtained using both MRM and GCV methods as described in Sec. 2.2.3 and 2.2.4 respectively.



Figure 2.3: Gelatin phantom used in the experimental studies [42, 43, 60].

### 2.3.2 Gelatin Phantom Experiment

For objective verification of the method, the experimental data collected using a gelatin phantom was used. A multi-layer cylindrical gelatin phantom of diameter 86 mm, height 25 mm was fabricated following the procedure as explained in Ref. [56] and mixtures of 80% of deionised water and 20% of gelatin (G2625, Sigma Inc) along with India ink for absorption and Titanium oxide ( $TiO_2$ ) for scattering was used. These layers of gelatin were successively hardened to form a 3-layer phantom to mimic typical breast tissue. The outer layer had optical properties of  $\mu_a = 0.0065 \text{ mm}^{-1}$ ,  $\mu'_s = 0.65 \text{ mm}^{-1}$  with a thickness of 10 mm, mimicking the fatty layer of the breast. The inner layer, mimicking the fibro-glandular layer, had properties of  $\mu_a = 0.01 \text{ mm}^{-1}$ ,  $\mu'_s = 1.0 \text{ mm}^{-1}$ . To mimic

the tumor characteristics, along the Z direction a cylindrical hole having a radius of 8 mm and height of 24 mm was made and filled with intra-lipid mixed with India ink to act as an absorptive target having the optical properties  $\mu_a = 0.02 \text{ mm}^{-1}$ ,  $\mu'_s = 1.2 \text{ mm}^{-1}$  and the optical properties were validated using 785 nm wavelength laser diode as the source. The log-amplitude data collection of the exiting light were collected using only one layer of fibers placed at the middle of the cylinder(at  $z = 0 \text{ mm}$ ). The collected data was calibrated using the coarser mesh that was used in the simulation studies using the procedure explained in Ref. [57]. The adipose layer optical properties were used as initial guess for reconstruction procedures.

All computations were carried out on a Linux workstation with dual quad-core Intel Xeon processor 2.33GHz with 64 GB RAM. The algorithms were implemented in MATLAB.

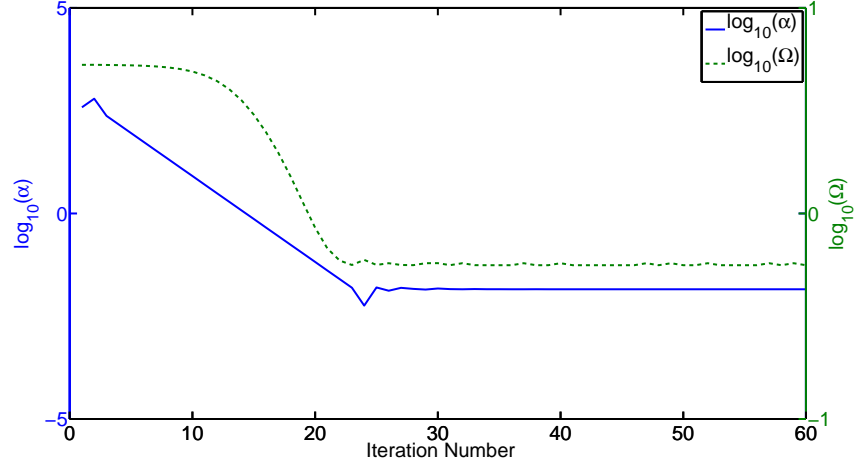


Figure 2.4: Plot of the estimated regularization parameter ( $\alpha$ ) using MRM and the corresponding data-model misfit ( $\Omega = ||y - G(\mu_a)||_2^2$ ) as a function of the inner iteration number for the first global iteration of the results presented in Fig. 2.5.

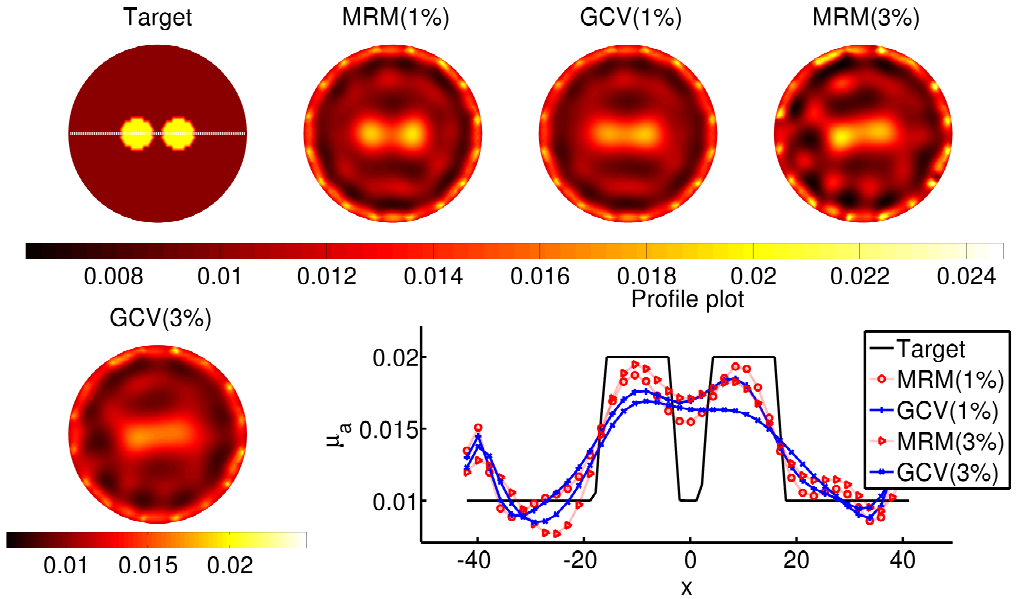


Figure 2.5: Comparison of reconstruction performance using the two methods discussed in this work for the two circular targets of dimension 7.5 mm radius separated by a distance of 5mm with numerically generated 1% and 3% noisy data. The reconstructed images obtained along with corresponding method with the percentage of the noise added (given on top of image) are given along with the target image. One-dimensional cross-sectional plot of  $\mu_a$  along the line (shown on the target) for the target and reconstructed results presented here are given in the second row.

Result	MRM Method	GCV Method
Fig. 2.5 (1% Noise-case)	55.42 (3)	12.20 (3)
Fig. 2.5 (3% Noise-case)	104.88 (4)	12.15 (3)
Fig. 2.8 (Gelatin Phantom)	167.75 (4)	12.36 (3)

Table 2.1: Comparison of total computational time (in seconds) including the overhead, for three reconstruction results (first column) presented in the Fig. 2.5 for the 1% noise case. The corresponding method is given in the first row of the table. The total number of iterations taken to converge are given in the parenthesis.

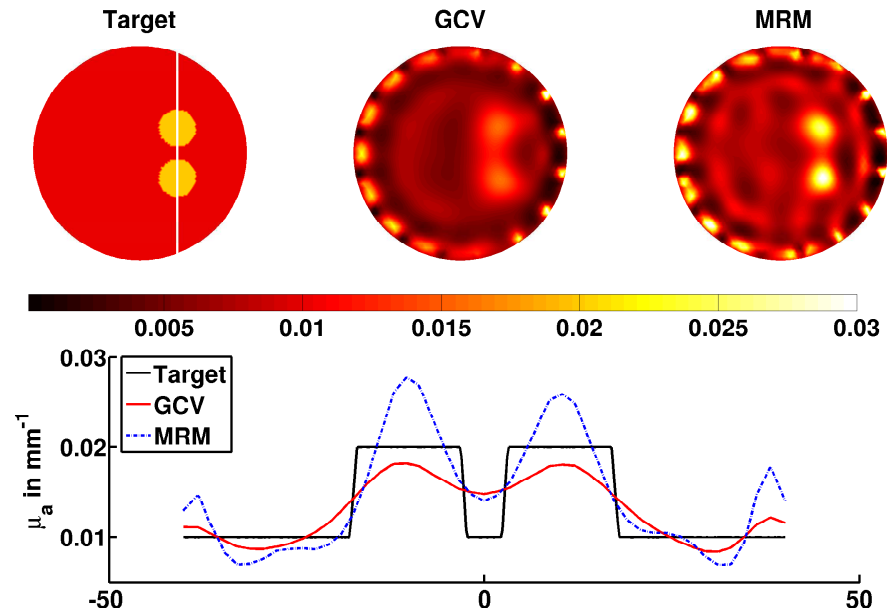


Figure 2.6: Similar effort as Fig. 2.5 with the anomalies placed in an asymmetric position for the case of simulation data with 1% noise.

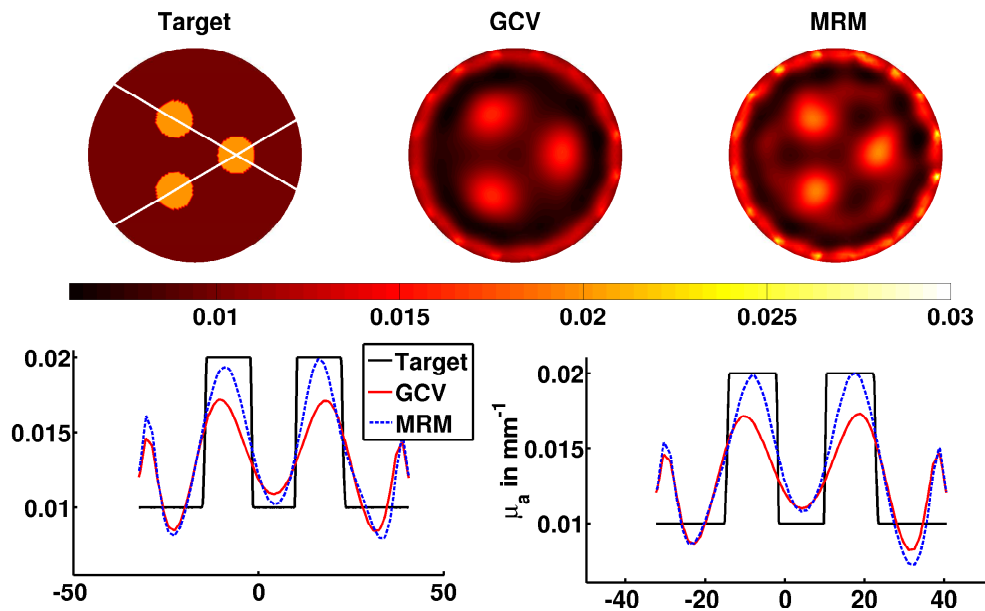


Figure 2.7: Similar effort as Fig. 2.5 with the three anomalies placed in the position as shown in the figure labeled as ‘target’ with 1% noise added to data.

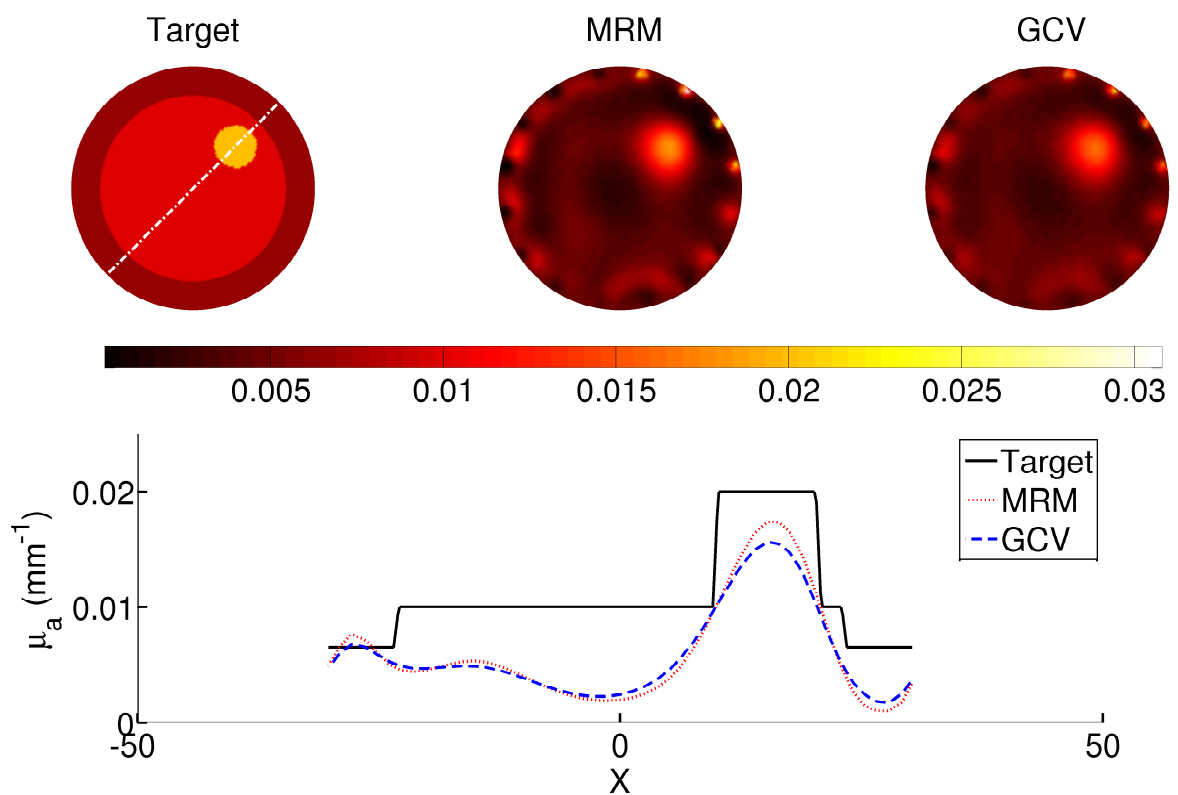


Figure 2.8: Similar effort as Fig. 2.5 for the case of experimental gelatin phantom data.

## 2.4 Comparison of Image Reconstruction Results

Initial results to show that regularized MRM is equivalent to standard (direct) reconstruction are given in Fig. 2.2. The reconstruction methods that were used are given on top of each  $\mu_a$  distribution. A one-dimensional profile plot across the dotted line as shown in Target  $\mu_a$  is given in the second row of Fig. 2.2. The results indicate that for a given  $\alpha$  the iterative technique (MRM) and direct inversion are equivalent. Note that the number of iterations that were needed to converge in both cases were 13 and in case of MRM at each iteration included about 400 inner iterations. From results shown in Fig. 2.2, it can be clearly seen that the reconstructed  $\mu_a$  distribution using MRM matches with the one obtained using the standard method within 2% error, assuring that the solution obtained using MRM is numerically equivalent to the solution obtained using direct inversion (Euler equation). Using the standard reconstruction method, the computation time needed per iteration was 0.829 s and for MRM, it was 0.688 s.

In the second case of numerical experiments using 1% and 3% noisy data, the regularization parameter was found using both MRM and GCV methods as outlined in Sec. 2.2.3 and 2.2.4. The obtained reconstruction results are given in Fig. 2.5. The one-dimensional cross-sectional plot for the obtained results similar to Fig. 2.2 is given in the second row of Fig. 2.5. The MRM-based estimation of regularization for the 1% noisy data case has resulted in convergence in 4 iterations with  $\alpha$  being 1.3e-2, 1.1e-3, 2.7e-4, and 6.0e-6, for the GCV the convergence was achieved in 3 iterations with  $\alpha$  being 1.4e-2, 1.2e-2, and 1000. Note that for the 3% noisy data case, the obtained  $\alpha$  values were in the same numerical range. The results also indicate that the resolution characteristics were better using MRM based regularization parameter compared to its counter part. The number of iterations that were required to find the  $\alpha$  in either cases were highly dependent on the initial guess. Similar trend is followed for the next two cases also and the reconstruction results along with the one-dimensional cross-sectional profile plots are shown in the Figs 2.6 and 2.7.

The results that were obtained using estimated  $\alpha$  with MRM and GCV methods for the case of gelatin phantom data are given in Fig. 2.8. In here as well, the MRM-based regularization parameter selection resulted in convergence in 4 iterations with  $\alpha$  being 1.1e-2, 2.6e-3, 8.1e-4, and 6.0e-6. Correspondingly the convergence for GCV-based method was in 3 iterations, with  $\alpha$  being 8.0e-3, 7.8e-3, and 1.69. The one-dimensional cross-sectional plot along the dashed line in the target are given in the second row of Fig. 2.8. The results indicate that the performance of the MRM to find an optimal  $\alpha$  is better compared to GCV based method as the reconstructed target  $\mu_a$  value is more close to the expected one.

## 2.5 Discussion

The diffuse optical tomographic image reconstruction problem is ill-posed in nature due to multiple scatterings of near infrared light. Many reconstruction methods were proposed for improving the reconstruction accuracy, making it more quantitative in nature, which uses structural and/or functional information [40, 43, 67–69]. The quantitative accuracy of the results are dependent on the choice of regularization, making the problem of finding optimal  $\alpha$  in an automated way highly relevant to the ongoing efforts. Moreover, such an automated method will remove the unwarranted bias in the reconstruction results due to heuristic choice of regularization parameter. Till now, the most successful methods in the literature includes GCV and L-curve method [70–72]. In this work, the proposed method is compared with the GCV-based approach and is found to be sub-optimal. The L-curve method is not considered in this work as it is known for the problems like diffuse optical tomography always provided overly-smooth solutions [70] as it can not exhibit a clear corner to find an optimal regularization parameter [71, 72].

Finding the regularization parameter using MRM method could also be achieved using Euler equations , but increases the computational complexity associated with it by an order ( $O(NN^2)$  versus  $O(NN^3)$ ). In case of GCV, the regularization parameter

increased abruptly before the last global iteration of the reconstruction procedure, resulting sub-optimal estimates of  $\mu_a$  compared to MRM-based method. This trend of GCV inability to find an optimal  $\alpha$  is also discussed in Ref. [71], where this is caused by either function being flat or display multiple minima, leading to sub-optimal choice of  $\alpha$ , causing over smoothing of reconstructed images. To show the inner iterative behavior of the proposed method, the semi-log plot of data-model misfit and the corresponding  $\alpha$  was plotted in Fig. 2.4 for 60 iterations for the set of results presented in Fig. 2.5 (first global iteration). These plots indicate that there is a clear convergence in finding  $\alpha$  and correspondingly the data-model misfit is also minimum for the optimal  $\alpha$ .

For the case of numerically generated 3% noisy data, the reconstruction results were poor in terms of resolution for the case GCV (Fig. 2.5), making the targets indistinguishable. For the MRM case, it is clearly evident that the reconstructed image quality is better in comparison to the result obtained using GCV-method (Figs. 2.5 2.6 and 2.7). This results also indicates that the spatial resolution in the reconstructed  $\mu_a$  image is higher by the usage of MRM method compared to the deployment of the GCV method.

Finding the optimal  $\alpha$  requires repeated solving of the forward problem, which might be computationally expensive in case of large problems, especially involving a large number of measurements. The additional step of finding the optimal  $\alpha$  through MRM method for the cases discussed in here, requires about 9.6 sec and for the GCV method it is 2.7 sec. This additional computational complexity added by the optimization procedure of finding optimal  $\alpha$  is justifiable as it removes the unwarranted bias in the reconstruction results due to either poor or desirable choice of  $\alpha$  heuristically and does not require any additional information in finding optimal  $\alpha$ . This computation time could be further reduced by the usage of GPU-based computing environments [73] which can speed up the computations in providing the optimal  $\alpha$  [61].

# Chapter 3

## Non-Quadratic Penalization in DOT

### 3.1 Introduction

To overcome the ill-posedness of the inverse problem in diffuse optical tomographic imaging and to obtain an unique solution, a penalty term is deployed in the estimation process. The penalty terms, also known as regularization schemes, not only stabilizes the solution, but also promotes faster convergence to the iterative solutions. More precisely, instead of only trying to minimize the data-model misfit, the objective function to be minimized for diffuse optical tomographic image reconstruction incorporates additional information about the image to be reconstructed by including a penalty term. Several penalty terms are proposed in the literature that can effectively be used to model the unknown optical property distribution [37, 40, 51, 67]. In multi-modal diffuse optical imaging systems, the structural information provided by the traditional imaging modalities has been incorporated into the penalty terms to improve diffuse optical image reconstruction [40]. The standard and the most simple method is the Tikhonov-type (quadratic) regularization, in which, the image quality is determined by the regularization parameter (scalar value). A higher value “over-smooths” the reconstructed image results in the loss of the image quality due to poor spatial contrast and resolution, whereas a lower value amplifies the high frequency noise [51, 75].

Even though often maligned [75] quadratic penalties provide a useful reduction in image noise over a large range of spatial resolution, non-quadratic potential functions as penalty terms may induce additional non-uniformities beyond the resolution effects. In this case, the models of the imaging domain has to be consistent with the actual image to be reconstructed [76–79]. In this chapter, a simple, yet effective, framework to incorporate the non-quadratic penalty terms is introduced for the inverse problem encountered in the diffuse optical tomography. Using this framework, three such non-quadratic penalty terms are deployed to show their usefulness in some special cases. Mainly the resolving power, robustness against noise-levels, and high contrast recovery of the proposed penalty functions are compared with the standard uniform quadratic regularization parameter. Moreover, the generalized cross-validation (GCV) method is incorporated into this framework for automated choice of regularization parameter for getting unbiased reconstruction results. The reconstruction results using different penalization schemes deployed in this chapter have been compared quantitatively via usage of both contrast resolution and contrast-to-noise ratio figures of merit. As emphasis of this chapter is on investigating the effect of non-quadratic penalty functions on the image reconstruction, the discussion is limited to continuous-wave (CW) case. In this the amplitude of the light is the boundary data collected from which the unknown optical absorption coefficient distribution is recovered.

## 3.2 Non-Quadratic Penalization : Framework

The inverse problem solving involves estimation of the unknown optical property distribution using the limited number of continuous-wave boundary measurements via a model-based approach. This is typically an iterative procedure, where the experimental measurements are matched iteratively with modeled-data in the least-squares sense over the range of  $\mu_a$ . The inverse problem is popularly solved as an optimization problem [21, 22, 24, 40, 45, 49, 50, 55], involves direct calculation of the Jacobian ( $\mathbf{J}$ ) (also known as the sensitivity matrix) with the help of forward model, followed by solving

linear system of equations to estimate the update in the optical properties. The details are explained in the previous chapter (Chapter 2).

In the linearized objection function instead of Tikhonov regularization term, which is quadratic ( $\ell_2$ -norm-based), one can deploy the non-quadratic penalty terms [76, 77, 79]. Some of these penalties are given in Table-3.1 (including the  $\ell_2$ -norm-based one) with  $\sigma_{\Delta\mu_a}^2$  representing the variance in  $\Delta\mu_a$ . Typically, these penalty terms are added to stabilize the solution, thus ensuring the convergence [78, 101] and removing high-frequency components [51, 67]. Different penalty functions model the distribution of the update, in turn modeling the absorption coefficient of the domain. The inclusion of  $\sigma_{\Delta\mu_a}^2$  in the update equation assists in controlling the reconstructed image quality at each iterative step. The generalized objective function in this case can be written as

$$\Omega = \frac{1}{2} \|\delta - J\Delta\mu_a\|_2^2 + \lambda \rho(\Delta\mu_a) \quad (3.1)$$

where  $\rho(\Delta\mu_a)$  is one of the penalty function given in Table-3.1. Minimizing the above objective function with respect to  $\Delta\mu_a$  and equating the first-order derivative to zero leads to

$$-J^T(\delta - J\Delta\mu_a) + \lambda \rho'(\Delta\mu_a) = 0 \quad (3.2)$$

Penalty Function	$\rho(\Delta\mu_a)$	$\rho'(\Delta\mu_a) = \frac{\partial\rho(\Delta\mu_a)}{\partial\Delta\mu_a}$	$D_{\Delta\mu_a} = \frac{\rho'(\Delta\mu_a)}{\Delta\mu_a}$
<b>Quadratic</b> ( $\ell_2$ )	$\frac{1}{2} \left( \frac{\Delta\mu_a}{\sigma_{\Delta\mu_a}} \right)^2$	$\left( \frac{\Delta\mu_a}{\sigma_{\Delta\mu_a}^2} \right)$	$\frac{1}{\sigma_{\Delta\mu_a}^2}$
<b>Absolute Value</b> ( $\ell_1$ )	$\left  \left( \frac{\Delta\mu_a}{\sigma_{\Delta\mu_a}} \right) \right $	$\frac{sgn(\Delta\mu_a)}{\sigma_{\Delta\mu_a}}$	$\frac{1}{\sigma_{\Delta\mu_a}  \Delta\mu_a }$
<b>Cauchy</b>	$\frac{1}{2} \ln \left[ 1 + \left( \frac{\Delta\mu_a}{\sigma_{\Delta\mu_a}} \right)^2 \right]$	$\frac{\Delta\mu_a}{\sigma_{\Delta\mu_a}^2 + \Delta\mu_a^2}$	$\frac{1}{\sigma_{\Delta\mu_a}^2 + \Delta\mu_a^2}$
<b>Geman-McClure</b>	$\frac{1}{2} \left[ \frac{\Delta\mu_a^2}{\sigma_{\Delta\mu_a}^2 + \Delta\mu_a^2} \right]$	$\frac{\Delta\mu_a \sigma_{\Delta\mu_a}^2}{\sigma_{\Delta\mu_a}^2 + \Delta\mu_a^2}$	$\frac{1}{(\sigma_{\Delta\mu_a}^2 + \Delta\mu_a^2)^2}$

Table 3.1: Different penalty functions and their derivatives that are deployed for estimation of optical properties using Eq. 3.4

Further simplification leads to the update equation,

$$\left[ J^T J + \lambda \frac{\rho'(\Delta\mu_a)}{\Delta\mu_a} \right] \Delta\mu_a = J^T \delta \quad (3.3)$$

Similar to the Eq. 1.20, the update equation for the  $i^{th}$  iteration becomes

$$\left[ \mathbf{J}_{i-1}^T \mathbf{J}_{i-1} + \lambda_i \mathbf{D}_{\Delta\mu_a^{i-1}} \right] \Delta\mu_a^i = \mathbf{J}_{i-1}^T \delta_{i-1} \quad (3.4)$$

where,  $(\mathbf{D}_{\Delta\mu_a^{i-1}})$  is a diagonal penalty-matrix defined as,

$$(D_{\Delta\mu_a})_{ii} = \left( \frac{\rho'(\Delta\mu_a)}{\Delta\mu_a} \right)_i \quad \text{for } i = 1, 2, \dots, NN \quad (3.5)$$

where  $NN$  represents the number FEM nodes reconstructed. Actual functional forms of  $D_{\Delta\mu_a}$  of some of the penalty function are listed in the fourth column of Table-3.1.

The first row of the Table-1 gives the  $\ell_2$  norm based penalization and the last column of the first row gives the diagonal matrix  $D_{\Delta\mu_a}$

$$(D_{\Delta\mu_a})_{ii} = \frac{1}{\sigma_{\Delta\mu_a}^2} \quad \text{for } i = 1, 2, \dots, NN \quad (3.6)$$

where  $\sigma_{\Delta\mu_a}^2$  represents the variance of the  $\Delta\mu_a$  and this makes the  $D_{\Delta\mu_a}$  a scalar matrix. Now this gives the update equation which is same as the traditional update (refer to the Eq. 1.20) wherein regularization parameter scales the  $D_{\Delta\mu_a}$ . On careful observation, for the  $\ell_2$  norm based penalization finding the update using Eq. 1.20 requires only the knowledge of the variance of the update and it is part of the regularization parameter making the  $D_{\Delta\mu_a}$  an scalar multiple of the identity matrix.

Different functional forms of  $\rho(\Delta\mu_a)$  along with the traditional  $\ell_2$  norm-based functions is listed in second column of Table-3.1 and in this table, note that the standard deviation of the  $\Delta\mu_a$  is represented as  $\sigma_{\Delta\mu_a}$ .

Similarly if one takes different non-quadratic penalty functions as given in Table-3.1, we can get different forms of the diagonal matrix  $D_{\Delta\mu_a}$  in the update equation (Eq. 3.4). For any generic penalty function it is not possible to find the diagonal matrix  $D_{\Delta\mu_a}$ , as  $\Delta\mu_a$  itself is the unknown, and here, we are using information obtained from the previous iteration to find the diagonal matrix and for starting the iteration we are using a single scalar value for all the node which is obtained from the GCV method explained in the next subsection. So, the modeling parameters for defining all the penalty functions in this approach is progressively made from the previous update and is independent of any heuristics.

Note that the first iteration of the reconstruction scheme is same for all cases, where we use standard quadratic penalty and the regularization parameter used is 0.01. From second iteration onwards the penalty terms as given in Table-3.1 are deployed and the regularization parameter ( $\lambda_i$ ) is automatically chosen using the GCV method.

### 3.2.1 Optimal Regularization Parameter using GCV

The Generalized Cross-Validation (GCV) method is the most popular method for estimating the optimal regularization parameter in the ill-posed inverse problems [53, 54]. The main advantage of this method is that it does not require the accurate estimation of the noise-level ( $\sigma^2$ ) present in the system for finding the optimal regularization parameter. Using GCV method, obtaining an estimate for the regularization parameter used in Eq. 3.4 is achieved by minimizing a continuous function  $G(\lambda)$ , with  $\lambda > 0$ , which is given by

$$G(\lambda) = \frac{\frac{1}{NN}||(I - A(\lambda))\delta||_2^2}{\left[\frac{1}{NN}trace(I - A(\lambda))\right]^2} \quad (3.7)$$

where,

$$A(\lambda) = \left[ \mathbf{J}_{i-1} \left( \mathbf{J}_{i-1}^T \mathbf{J}_{i-1} + NN \cdot \lambda \cdot \mathbf{D}_{\Delta\mu_a^{i-1}} \right)^{-1} \mathbf{J}_{i-1}^T \right] \quad (3.8)$$

where *trace* represents the trace of the matrix (sum of the diagonal entries). Since there exists an optimal regularization [80] or at least a suboptimal regularization for

a noisy-data, a direct line search methods can be applied to find the optimal  $\lambda$  which minimizes the  $G(\lambda)$ . For finding such an optimal  $\lambda$ , a gradient-free simplex method type algorithm [66, 74] is used due to its computational compactness.

## 3.3 Experimental Studies

### 3.3.1 Numerical Experiments

In order to investigate the different characteristics of the reconstructed images obtained as a result of using different penalty functions, three numerical experiments are conducted. The imaging domain is circular in shape having a radius of 43 mm, where the source/detector fibers are placed on the boundary. The optical properties of the background are at  $0.01 \text{ mm}^{-1}$  for the absorption coefficient and  $1.00 \text{ mm}^{-1}$  for the reduced scattering coefficient. For the generation of the experimental amplitude measurements( $y = \ln(I)$ ) a fine finite element mesh having 10249 nodes(corresponding to 20160 triangular elements) was used, whereas for the generation of modeled-data  $G(\mu_a)$  a coarser finite element mesh with 1785 nodes (corresponding to 3148 triangular elements) was used. The measurement setup consisted of equi-spaced 16 fibers arranged along the circumference of the circular domain. When one fiber is used at a time as the source of NIR light then the remaining 15 fibers act as detector, resulting in 240 ( $16 \times 15$ ) measurements. To mimic the experimental conditions, Gaussian-type modeling of the source with full width at half maximum (FWHM) of 3 mm was used.

Initially, two circular absorbing targets are placed along x-axis with 5 mm separation and equidistant from the centre of the circular domain with contrast of 2:1 compared to the background  $\mu_a$  value. The target (expected)  $\mu_a$  distribution is given in Fig. 3.1 (top-left corner). The numerically generated data using fine mesh was added with 1% and 3% white Gaussian noise to mimic typical experimental scenario. One more case in which a centrally absorbing target with high contrast of 4:1 when compared with the background  $\mu_a$  was considered as the next test problem. The expected target distribution is given in the top-left most corner of Fig. 3.2. In this case, numerically generated data was

added with only 1% white Gaussian noise. The next test problem had two rectangular absorbers placed horizontally (centered at [0,-14 mm]) and vertically (centered at ([ -10 mm, 0])) to get a L-shaped target (shown in Fig. 3.4, top-left corner). The absorption contrast of the target is 2:1. Similar to earlier case, 1% white Gaussian noise is added to the numerical data. In all cases, a data-calibration has been performed to remove biases introduced due to irregularities in modeling source/detectors [57].

In order to effectively asses the reconstruction performance of different penalization, a numerical experiment involving a typical MRI-NIR human breast mesh is considered. The segmented high resolution MRI images clearly shows three breast regions and the corresponding optical properties of the tissue types that are used for simulation are  $\mu_a = 0.01 \text{ mm}^{-1}$  for the fatty region;  $\mu_a = 0.015 \text{ mm}^{-1}$  for fibro-glandular; and tumor with  $\mu_a = 0.02 \text{ mm}^{-1}$ . The target distribution of the same is shown in the left top corner of the Fig. 3.6. The  $\mu'_s$  is assumed to be known and kept constant at  $1 \text{ mm}^{-1}$  throughout this imaging domain also. The mesh used for the data collection is a fine mesh with 4876 nodes (corresponding 9567 triangular elements) and 1% Gaussian noise is added to mimic the real-life condition. For the reconstruction a coarse mesh with 1969 nodes (corresponding 3753 triangular elements) was used.

### 3.3.2 Gelatin Phantom Experiment

The same gelatin phantom data that was described in Sec. 2.3.2 was also utilized here. The finite element mesh specifications were also same as in Sec. 2.3.2.

### 3.3.3 Quantitative Analysis

To better assess the performance of different penalty functions deployed in the test cases presented in this work, a quantitative [81, 82] analysis was undertaken using the metrics relative error (RE) and Pearson correlation (PC). As the studies involved here are numerical in nature, these metrics could be easily computable.

The relative error,  $RE$ , is a quantitative metric to measure the deviation of the reconstructed image from the target image and is defined as

$$RE = \left[ \frac{\|([\mu_a]_{TRUE} - [\mu_a]_{RECON})\|_2}{\|([\mu_a]_{TRUE})\|_2} \right] \times 100 \quad (3.9)$$

where  $[\mu_a]_{TRUE}$  and  $[\mu_a]_{RECON}$  respectively represents the target and the reconstructed images. The lesser the  $RE$  the better is the reconstruction performance of the penalty function.

Pearson Correlation,  $PC$ , quantitatively [83] measures the detectability in the reconstructed images by measuring the linear correlation between the target and the reconstructed image and is defined as

$$PC([\mu_a]_{TRUE}, [\mu_a]_{RECON}) = \frac{COV([\mu_a]_{TRUE}, [\mu_a]_{RECON})}{\sigma([\mu_a]_{TRUE})} \quad (3.10)$$

where  $COV$  is the covariance and  $\sigma$  indicates the standard deviation. The higher the PC value, the better is the detectability of the anomalies in the imaging domain.

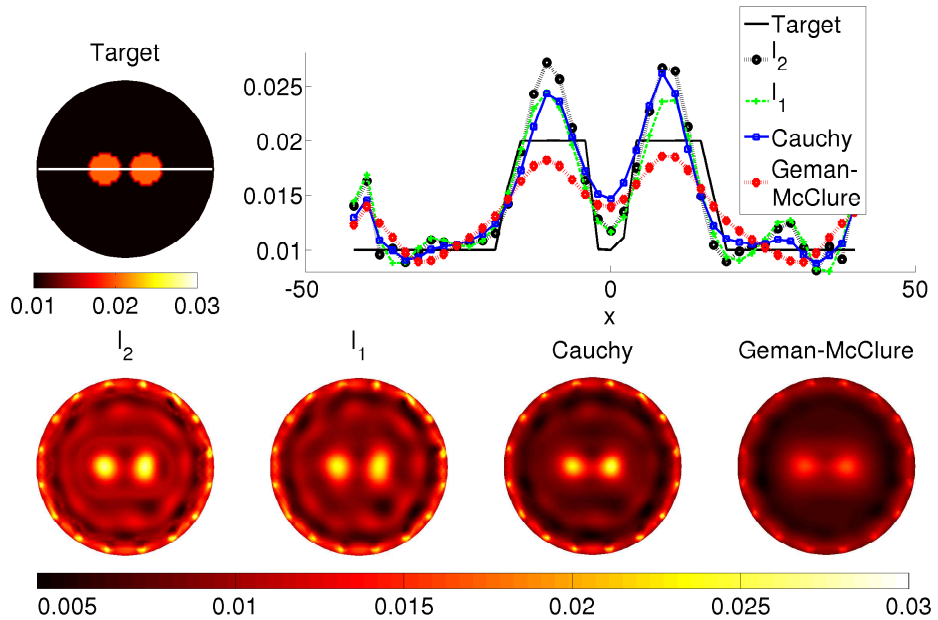


Figure 3.1: Reconstructed images using the penalization functions discussed in this chapter in the numerical experiment with 1% noisy data involving the target distribution given on top-left corner of the figure. The penalization functions are given correspondingly on top of each reconstructed image. The one-dimensional cross-sectional profile along the solid line of the target distribution is given on the top-right corner.

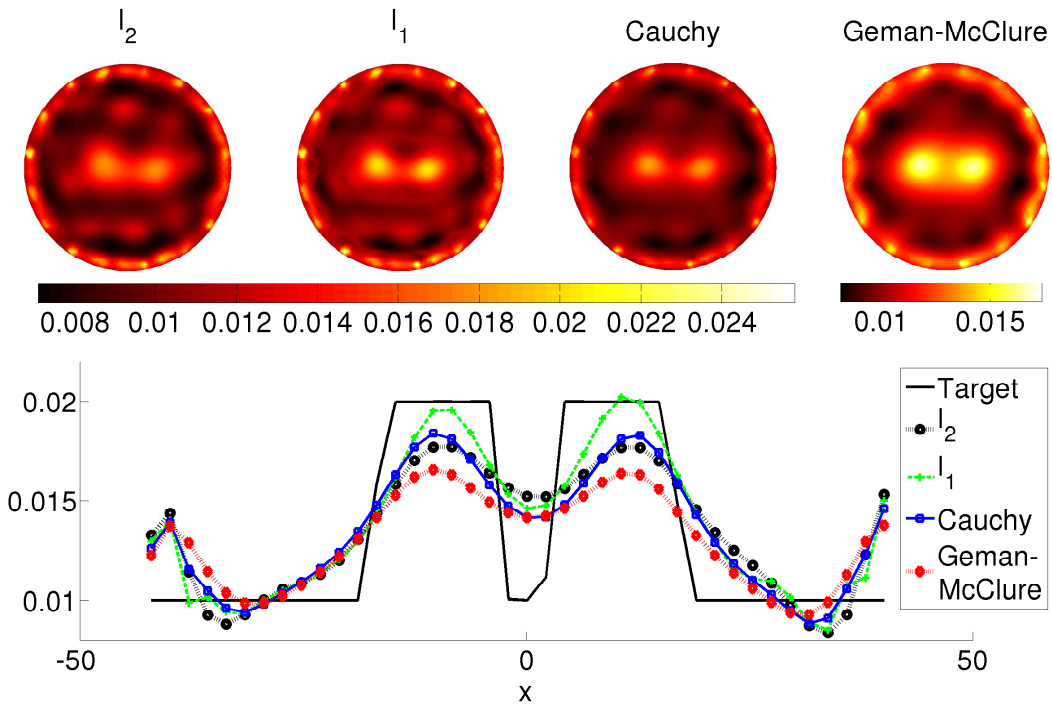


Figure 3.2: Similar effort as in the Fig. 3.1. except data noise level being 3%, the target distribution is same as Fig. 3.1.

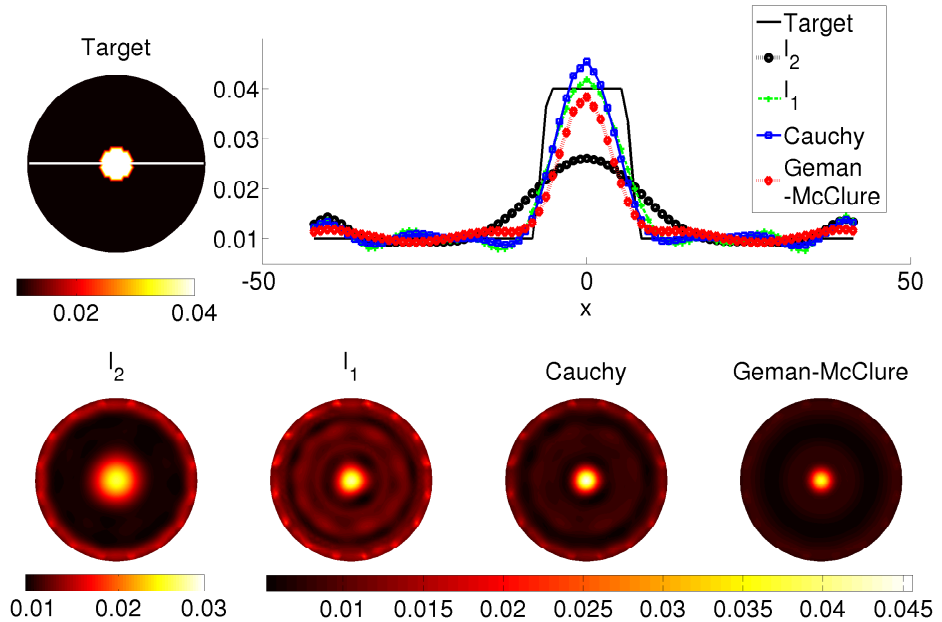


Figure 3.3: Similar effort to Fig. 3.1 except the target is located at the centre having contrast of 4:1.

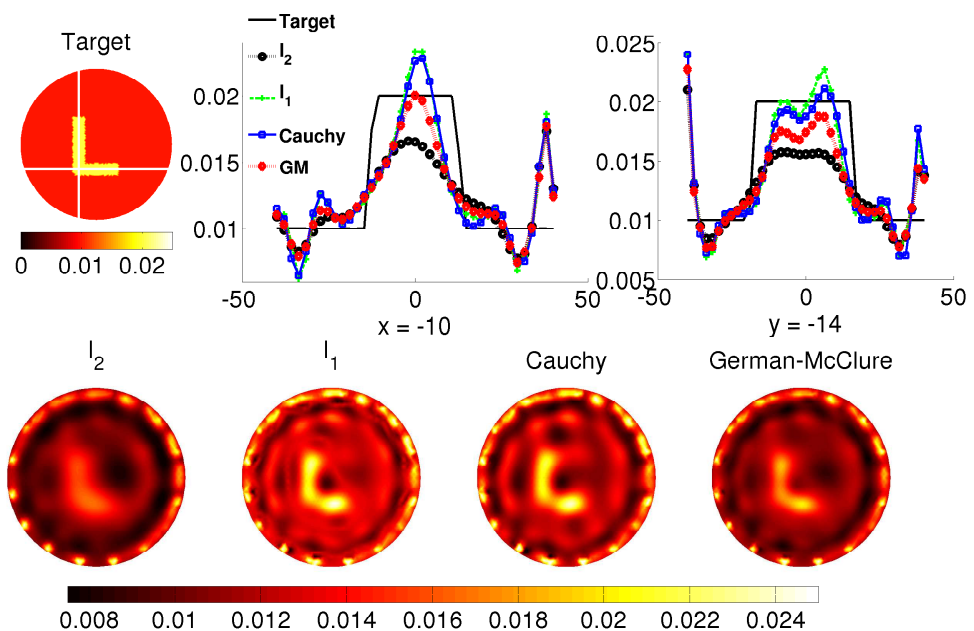


Figure 3.4: Similar effort to Fig. 3.1 except the target is L-shaped.

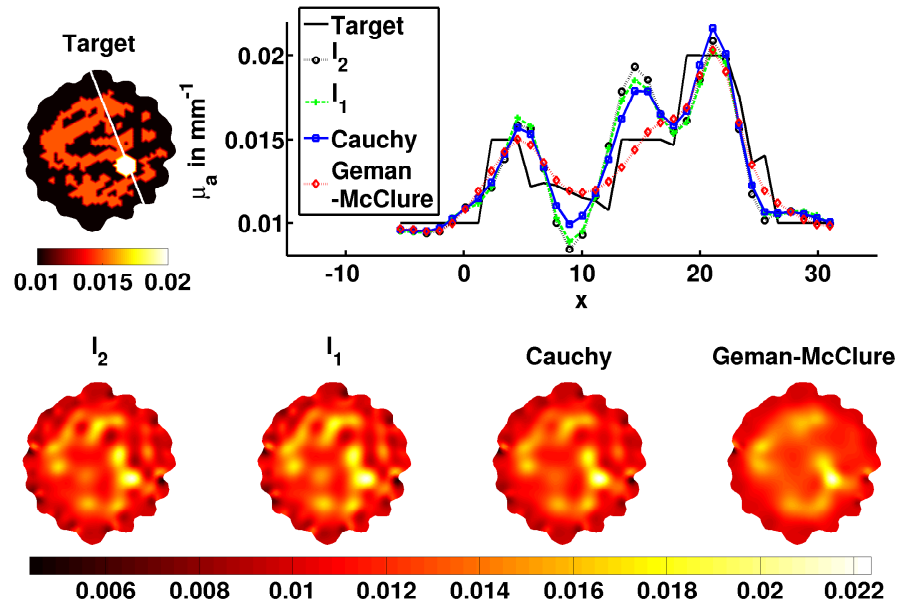


Figure 3.5: Reconstructed optical images with various penalty functions listed in Table-3.1 using realistic MRI derived patient mesh. The one-dimensional cross-sectional profile along the solid line of target distribution is given on the top-right corner.

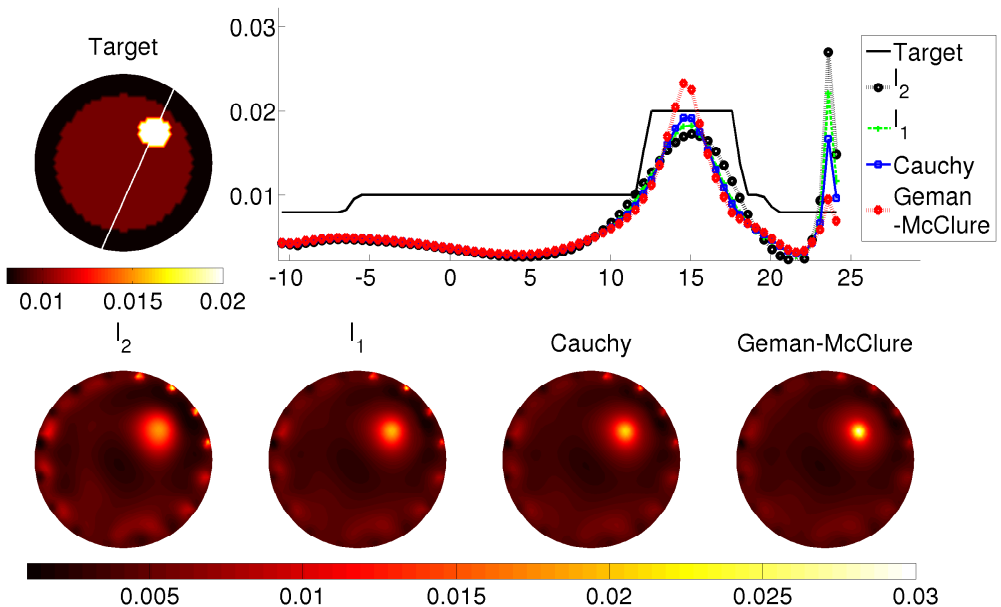


Figure 3.6: Reconstruction results obtained using multi-layered gelatin phantom experimental data.

## 3.4 Results

The reconstruction results in the numerical experiment conducted using the target distribution having two-circular targets (top-left corner of Fig. 3.1) are given in Fig. 3.1 and 3.2 for 1% and 3% noisy data cases respectively. The penalty functions used are given on top of each reconstructed image and the one-dimensional cross-sectional profile along the solid line of the target distribution is also given in the same figures. The corresponding penalty function forms are given in Table-3.1. The RE and PC quantitative metrics for the analysis of these results are given in Table-3.2 and 3 respectively. These results indicate that the  $\ell_2$ ,  $\ell_1$ , and Cauchy penalty function performance in resolving the anomalies is comparable, while Geman-McClure has the best performance compared to others. But even though the reconstruction is not visually showing good performance for the Geman-McClure, the RE value is the lowest as it is evident from the profile plot that the variation from the target distribution is far less when compared with other penalty functions.

The numerical experimental results (1% noisy data) of the high-contrast target placed at the center of the imaging domain is given in Fig. 3.3 along with the one-dimensional cross-sectional profile. Similar to earlier case, the quantitative metrics that analyze the results are given in Tables 3.2 and 3.3. As expected, it is clearly seen how the non-quadratic penalization gives better reconstruction than the traditional  $\ell_2$ -based penalization both visually and also by the one-dimensional line-profile plot shown in the same figure.

In the Fig. 3.4, the reconstruction results of L-shaped target is provided using the penalty functions described in this chapter. Similar to earlier results, the corresponding figures of merit of the reconstructed results are given in Tables 3.2 and 3.3. These results indicate, in terms of quantitative metrics, that  $\ell_2$  and  $\ell_1$  -based penalty performance is inferior compared to others and, non-convex penalty functions (Cauchy and Geman-McClure) performance is superior among all.

The reconstruction results with patient mesh obtained from MRI images using various penalty functions are given in the Fig. 3.5 along with the one-dimensional cross-sectional profiles. Tables 3.2 and 3 also have the quantitative comparison of these reconstruction results. Quantitatively the performance of all penalty functions is similar, with Geman-McClure result shows that it is effective in suppressing the background artifacts (also true for the results presented in Fig. 3.5). Further, the shape recovery is more closely following the expected distribution (Line profile of Fig. 3.6). The experimental gelatin phantom reconstruction results using various penalty functions are given in the Fig. 3.5 along with the one-dimensional cross-sectional profiles. Tables 3.2 and 3.3 also have the quantitative comparison of these reconstruction results. Quantitatively the performance of all penalty functions is similar, but Geman-McClure result shows that it is effective in suppressing the boundary artifacts (also true for the results presented in Fig. 3.3).

Figures	$\ell_2$	$\ell_1$	Cauchy	Geman-McClure
Fig. 3.1	30.3253	29.8520	26.7255	20.6825
Fig. 3.2	25.6591	24.9072	22.6244	20.0364
Fig. 3.3	29.1088	29.7643	27.4685	19.4516
Fig. 3.4	32.5844	30.0740	28.3723	29.2519
Fig. 3.5	35.6552	35.4859	31.5659	25.5824
Fig. 3.6	16.9519	16.9585	15.8667	15.2391

Table 3.2: Quantitative comparison of relative error ( $RE$ , Eq. 3.9) of the reconstruction results using the penalty functions discussed in this chapter.

Figures	$\ell_2$	$\ell_1$	Cauchy	Geman-McClure
Fig. 3.1	0.4794	0.4744	0.4825	0.5270
Fig. 3.2	0.4258	0.4599	0.4781	0.5283
Fig. 3.3	0.3884	0.4045	0.3907	0.5373
Fig. 3.4	0.6762	0.7193	0.7552	0.7944
Fig. 3.5	0.3516	0.3506	0.3321	0.3744
Fig. 3.6	0.6495	0.6502	0.6847	0.7046

Table 3.3: Quantitative comparison of Pearson correlation ( $PC$ , Eq. 3.10) of the reconstruction results using the penalty functions discussed in this chapter.

### 3.5 Discussion

The inverse problem of estimating the internal distribution of tissue optical properties in NIR diffuse optical tomography is a challenging task and involves using advanced numerical techniques to get reasonable estimates. The ill-posedness encountered in the inverse problem is compensated by using penalty/regularization terms to get an unique solution. Often, these penalties dictate the reconstructed image characteristics. Many penalties have been proposed in the literature, more often they are based on the prior information available to the user about the imaging domain and data-noise level [43, 68, 84, 85]. In here, the frame work was more tailored towards usage of non-quadratic penalties especially in case where no prior information, including the structural information, about the tissue under investigation and data-noise level is available. The proposed generalized framework can easily incorporate any penalty function, including the standard quadratic penalty, for reconstruction of optical properties. Also, the proposed scheme is independent of any heuristics imposed by the choice of regularization parameter( $\lambda_i$ ), which is automatically estimated in this method using the the generalized cross-validation (GCV) method.

Even though there are only three other penalties, other than the standard quadratic penalty, is discussed in this work, the proposed frame work can be extended to include any generic penalty function. The quantitative analysis of the results via the figures

of merit has provided some insights into the deployment of appropriate penalties for a given problem at hand. For example, if the imaging problem demands suppression of boundary artifacts in the reconstructed images (Figs. 3.5), usage of either traditional quadratic ( $\ell_2$  norm) penalties should be encouraged. On the other hand, if one is interested in the recovery of the shapes of the target, the usage non-quadratic penalty should be discouraged (Fig. 3.4). For the case of high-contrast target (Fig. 3.3), the traditional method ( $\ell_2$ -norm based) may not be optimal as it encourages smooth solutions compared other non-quadratic penalties. Also, it is evident from other results that the non-convex penalties (Cauchy and Geman-McClure) may be the optimal one for the cases discussed in this work, as they promote sparse solutions. The Geman-McClure penalty function yields a sparser result compared to Cauchy [76]. By the figures of merit, one could see that Geman-McClure performance is superior compared to others, visually also the Geman-McClure produces better appealing results by reducing the background artifacts (Figs. 3.4 and 3.6).

Even though the cases considered here are limited in nature, the aim of this chapter is show that non-quadratic penalization can improve the diffuse optical tomographic image reconstruction by providing additional information/feedback into the minimization scheme.

# Chapter 4

## Refractive Index Variation in IG-DOT

### 4.1 Introduction

The numerical iterative models and optimization schemes explored in the literature have been two dimensional (2D) only, even though the light propagation is in the three dimensions [40], mostly because of computational limitations. These 2D image reconstruction implementations are evaluated with data simulated by a 2D light transport model. One could hope to extend this approach to a tomographic scheme to reconstruct three-dimensional (3D) objects [86–88] by employing a tomographic setup that collects boundary data in a single plane at a time and then uses a 2D reconstruction program to produce the cross-sectional image in this plane, thereby forming a full 3D reconstruction as a series of 2D cross sections. Such a full 3D reconstruction solution with arbitrary parameter distributions, however, it is not obvious that a tomographic approach based on separate reconstructions of 2D slices is adequate because light will be scattered out of the imaging plane, and measurements will therefore be affected by the distribution of optical coefficients above and below the imaging plane. This is a fundamental difference to imaging modalities such as x-ray-computed tomography [86] , where scatter is negligible or can be eliminated and where 2D reconstructions from single-plane data are

therefore appropriate.

The full 3D reconstructions have been limited to semi-analytic methods that are known to less accurate for non-linear inverse problems [86]. A full 3D image-reconstruction scheme for optical tomography can be made as a natural extension of 2-D algorithm. [87] A full 3D reconstruction scheme that can be applied to data obtained in experimental measurements which employs a 3D light transport forward model that correctly describes the physics of the experimental setup used for the acquisition of the data it reconstructs its images from. Because the high degree of scattering in optical imaging does not allow one to confine photon propagation 3D models are necessary. The 3D model thus overcomes the problems of 2D models that necessarily ignore light propagation in the third spatial dimension. The successful application of the 2D algorithm to the 3D model significantly depends on the optical properties and sizes the ratio of the dimensions, more accurately of the object. Moreover, the 3D DOT inverse problem is more under-determined relative to the 2D case and has been found to reconstruct poor [40] quantitative estimates of the optical properties when compared to 2D results.

As stated in Chapter-1 (Sec. 1.3.2), the Image Guided Diffuse Optical Tomography (IG-DOT), also known as '*hard-priors*'), refers to the the image guidance is primarily in providing the structural information to perform the parameter reduction (known as '*hard-priors*') of the optical image reconstruction procedure [40, 43, 48, 89]. Due to the computational complexity of the soft-priors, the hard-priors approach is more sought after especially in three-dimensional (3D) diffuse optical imaging [40]. The hard-priors approach reduces the parameter space (optical properties) into the number of regions segmented from the high-resolution imaging modality [40, 43]. In the example of breast, this can be adipose (fatty), fibro-glandular, and tumor [36]. As the number of optical parameters to be reconstructed are equal to the number of segmented regions, the image reconstruction problem tends to be a better determined problem compared to the traditional reconstruction problem [40]. Earlier works presented in the literature have

exploited this in providing high-resolution diffuse optical images in IG-DOT [13, 14]. It was also shown that in the case of breast imaging, combining MRI with DOT, the IG-DOT was capable of eliminating the false-positives of MRI [13]. The effective image guidance in reconstructing diffuse optical images has been an active research area and in this study use of the region information to improve IG-DOT images by incorporating the refractive index (RI) variation is attempted.

The high-resolution images from traditional imaging modalities, in IG-DOT, are used to obtain the finite element meshes with segmented regions [14]. Identification/segmentation of these regions is an active area of research, as the uncertainties in the segmentation could influence the final outcome of the optical image reconstruction procedure [43, 48, 89]. Typically the diffusion equation (DE), which is valid for thick tissues, often solved on these meshes using finite element method (FEM). Even though RI of each segmented region is known to be different [90, 91], a uniform RI is typically used in solving the DE [36, 40, 43] leading to inaccurate modeling of NIR light propagation in tissue [93, 94]. This uniform modeling of RI is primarily due to the fact that the RI for the segmented regions is often not known, especially in *in-vivo*. Moreover, finding the RI distribution for the tissue under investigation should be posed as a new reconstruction problem, which is not so straight forward in the case of unknown optical properties [95]. Earlier investigations in breast imaging, limited to two-dimensions (also not in the context of IG-DOT), have shown that the uniform modeling of RI will have minimal effect on the estimated optical properties [94]. This chapter mainly aims to show that the approximation of internal RI values for the segmented regions (obtained from the literature) in IG-DOT will lead to improved estimates of optical properties. Note that the example cases shown in this chapter pertained to MRI-guided DOT for 3D breast cancer imaging. Results from the cases where the exact RI is assumed to be known *a-priori* are also presented for fair comparison along with the uniform RI cases. From the simulation studies, it will be shown that assuming uniform RI could lead to errors up to five times in terms of quantitation of optical properties in IG-DOT.

### 4.1.1 Estimation of Jacobian

Unlike the traditional approach, which uses adjoint method for calculation of Jacobian and mapping it to the regions using region mapper ( $\mathbf{R}$ ), Sec. 1.3.2, the simplest approach to calculate the Jacobian (in this case  $\tilde{\mathbf{J}}$  has been represented by  $\mathbf{J}$ ) is using perturbation approach, with

$$\mathbf{J} = \frac{G(\mu + \delta\mu) - G(\mu)}{\delta\mu}. \quad (4.1)$$

Here,  $\mu$  could be either  $D$  or  $\mu_a$  and the  $\delta\mu$  is 1% of the average value of  $\mu$ . Even though the traditional method of calculation of  $\mathbf{J}$  using adjoint method could also be employed resulting in dimension of  $2NM \times 2NN$  (where NN represents number of FEM nodes) with subsequently reducing it to  $2NM \times 2NR$  as given in Ref. [43]. Note that the perturbation approach is more memory efficient compared to the adjoint method, with later method requiring to store a large  $\mathbf{J}$  (with NN = 10,000 or more in 3D).

The RI modeling used in this chapter is described in detail in Ref. [93]. As stated earlier, the update equation is given by (using Levenberg-Marquardt (LM) minimization [40])

$$[\mathbf{J}^T \mathbf{J} + \lambda \mathbf{I}] (\Delta D, \Delta \mu_a) = \mathbf{J}^T (y - G(D, \mu_a)) \quad (4.2)$$

where  $\Delta D$  and  $\Delta \mu_a$  are the updates in  $D$  and  $\mu_a$ .  $\mathbf{J}$  is the Jacobian matrix, which is the first derivative of forward model ( $G$ ) with respect to optical properties  $(D, \mu_a)$  and has the dimension of  $2NM \times 2NR$  in the case of IG-DOT, where NM - number of measurements and NR - number of regions. The multiplication of factor of 2 in the measurements is because of treatment of amplitude and phase of signal separately. The information of NR is obtained through the image guidance provided by the traditional imaging modality (in here, it is MRI). In traditional DOT, NR is equal to number of FEM nodes present in the finite element mesh. In the case of breast imaging, the NR is equal to three, representing fatty (adipose), fibro-glandular, and tumor regions [36].  $\lambda$  in Eq. 4.2 represents the regularization parameter with a starting value of 1 (in this study) and reduced by  $10^{0.25}$  in every iteration [40]. The iterative procedure is stopped when the  $\Omega$  (Eq. 1.11) did

not improve by more than 0.001% in successive iterations.

### 4.1.2 Simulation studies using realistic 3D breast models

To study the effect of RI variation on the estimation of optical properties using hard-priors, we have considered totally six 3D meshes. These were obtained from segmenting and meshing of MRI T1-weighted images acquired on Dartmouth MRI-NIR imaging system [96] on patients with breast cancer. The procedure of volumetric meshing and segmenting of these MRI images is given in Ref. [14]. These patient 3D breast meshes are given an unique number (namely, 1915, 3007a, 1917, 501, 501c, and 1907) and each of FEM node in these meshes are labeled to uniquely identify the three regions (adipose, fibro-glandular, and tumor) of the breast. Along with these regions, the source/detector locations are also identified to perform the image reconstruction procedure. Totally 16 fiber bundles (source/detector) were placed in contact with skin in the middle plane of the breast (shown as filled circles on the target  $\mu_a$  distribution of Fig. 4.1 (second row, first column)) similar to Dartmouth MRI-NIR imaging system [96] and when one source is used as a source, rest acted as detectors, resulting in NM = 240 (16x15).

We have used the following properties (mimicking the typical breast [43, 91]) to generate numerical experimental data (with 1% noise added) to act as target meshes. The properties for adipose region:  $\mu_a = 0.01 \text{ mm}^{-1}$ ,  $\mu'_s = 1.0 \text{ mm}^{-1}$ , and RI = 1.467; fibro-glandular region:  $\mu_a = 0.015 \text{ mm}^{-1}$ ,  $\mu'_s = 1.5 \text{ mm}^{-1}$ , and RI = 1.389; and tumor:  $\mu_a = 0.02 \text{ mm}^{-1}$ ,  $\mu'_s = 2.0 \text{ mm}^{-1}$ , and RI = 1.390. Three different strategies were employed in this study in regard to show the effect of RI on the optical parameter estimation. They are given as follows along with the abbreviation for each of the strategy.

1. **RI-U:** The RI of each region is assumed to be uniform and equal to 1.467 (mimicking the adipose tissue values [91]).
2. **RI-E:** The RI of each region was same as used in the target mesh.
3. **RI-A:** The RI is approximated by taking the average values from the earlier reports

[90]- [94], [97], for each region. These are for adipose region: RI = 1.455; fibro-glandular region: RI = 1.4; and tumor: RI = 1.4.

Note that in all three strategies an uniform initial guess (same as the adipose) for the optical properties is used. Further in case of RI-U strategy, to know the improvement in the optical property estimation with multi-layer data, a numerical investigation that uses data from three fiber layers (fibers arranged similar to single plane) was also taken up. These three fiber layers are 10mm apart in the Z-direction (with one layer above and another below to the single layer) and when one fiber is used as a source, the fibers in the same fiber layer acted as detectors (three layers in-plane strategy in Ref. [43]), resulting in NM = 720 (3x16x15). As typical RI values of 1.4 and 1.33 are used in the literature under the uniform RI assumption an investigation with these values (along with 1.467) as test conditions is carried out to deduce a suitable RI that could be used in RI-U strategy. The FEM meshes used 12,000 nodes (up to 70,000) corresponding to 60,000 (up to 390,000) tetrahedral elements. The computations were carried out on a Linux workstation with dual quad-core Intel Xeon processor 2.33GHz with 64 GB RAM. The typical computation time for each iteration was  $\sim 3$  (up to 8) minutes.

Mesh	Method	Adipose		Fibro-glandular		Tumor	
		$\mu_a$	$\mu'_s$	$\mu_a$	$\mu'_s$	$\mu_a$	$\mu'_s$
<b>Target</b>	-	0.010	1.00	0.015	1.50	0.020	2.00
<b>1915</b>	<b>RI-U</b>	0.010	0.99	0.016	1.43	0.121	0.03
	<b>RI-E</b>	0.010	1.01	0.015	1.49	0.021	1.84
	<b>RI-A</b>	0.010	1.01	0.015	1.49	0.021	1.84
<b>3007a</b>	<b>RI-U</b>	0.011	0.99	0.015	1.54	0.019	2.07
	<b>RI-E</b>	0.010	1.00	0.016	1.43	0.019	2.10
	<b>RI-A</b>	0.010	1.01	0.016	1.46	0.019	2.11
<b>1917</b>	<b>RI-U</b>	0.010	1.00	0.020	1.48	0.020	1.99
	<b>RI-E</b>	0.010	1.00	0.017	1.40	0.020	2.10
	<b>RI-A</b>	0.010	1.01	0.018	1.42	0.020	2.10
<b>501</b>	<b>RI-U</b>	0.010	1.00	0.016	1.43	0.031	1.21
	<b>RI-E</b>	0.010	1.00	0.015	1.50	0.020	2.10
	<b>RI-A</b>	0.010	1.01	0.015	1.49	0.018	2.21
<b>501c</b>	<b>RI-U</b>	0.012	0.90	0.015	1.44	0.028	1.67
	<b>RI-E</b>	0.010	1.00	0.015	1.51	0.021	1.88
	<b>RI-A</b>	0.012	0.91	0.015	1.50	0.024	1.99
<b>1907</b>	<b>RI-U</b>	0.010	1.00	0.016	1.42	0.020	2.21
	<b>RI-E</b>	0.010	1.00	0.015	1.50	0.020	2.13
	<b>RI-A</b>	0.010	1.01	0.015	1.48	0.019	2.11

Table 4.1: Estimated optical properties (in  $\text{mm}^{-1}$ ) of each region using the three strategies discussed in Sec. 4.2.2 for six meshes.

RI	Adipose		Fibro-glandular		Tumor	
	$\mu_a$	$\mu'_s$	$\mu_a$	$\mu'_s$	$\mu_a$	$\mu'_s$
<b>RI = 1.467</b>	0.010	0.99	0.016	1.44	0.033	1.17
<b>RI = 1.4</b>	0.010	1.01	0.015	1.51	0.025	1.89
<b>RI = 1.33</b>	0.009	1.05	0.014	1.58	0.013	19.4

Table 4.2: Estimated optical properties (in  $\text{mm}^{-1}$ ) of each region of 1915 mesh using three fiber layers with RI-U strategy for RI = 1.467, 1.4. and 1.33. The target values are given in the second row of Table 4.1.

## 4.2 Discussion

The reconstructed  $\mu_a$  and  $\mu'_s$  distribution using 1915 3D breast mesh along with the target distribution (first column) are given in Fig. 4.1. The corresponding reconstruction strategies used to obtain the same are given on top of each column of Fig. 4.1. To analyze the results more carefully, the estimated optical properties for each region using three strategies mentioned in the Sec. 4.2.2 are compiled in Table 4.1. It is evident, from Table 4.2 and Fig. 4.1, that the estimated optical properties were erroneous when the RI was considered to be identical in all three regions of mesh, especially for cases of 1915, 501, and 501c. The error in estimating the optical properties,  $\mu_a$  &  $\mu'_s$ , in the tumor region of the cases mentioned are 505% & 98.5%, 55% & 39.5%, and 40% & 16.5% respectively (Table 4.1 and Fig. 4.1). Knowing the exact RI of each region gave better accurate results, but extracting the same information in *in-vivo* cases is difficult and typically requires a new inverse problem to be formulated [95]. As it is evident from Fig. 4.1 and Table 4.1 that even an approximation of RI (RI-A), which was obtained by taking the average value of the RI using the literature [90, 94, 97], lead to better estimation of optical properties. In all six cases, the performance of RI-A strategy is on par with the RI-E (where RI is assumed to be known *a-priori* for all regions). Moreover, in terms of computational complexity rather than using RI as an unknown, approximation of the same for different regions of tissue provides optimal solution.

Note that, when the same study was carried out in 2D (not shown here), the estimated optical properties were identical (variation of only  $\sim 5\%$ ). As there are more degrees of freedom for the light propagation in 3D compared to 2D (also 3D model being more accurate compared to 2D), the effect of reflection due to RI change might be more apparent in 3D, leading to changes in the estimated optical properties. Moreover, the number of parameters to be estimated in IG-DOT is equal to be number of regions and any modeling error (in here the RI change) has to reflect in estimated region optical properties. Note that in only 3 out of 6 cases considered here (Table 4.1) resulted in more erroneous results for the reconstruction strategy of RI-U. In other 3 cases, the

estimated optical properties were identical within 10%. The RI-A strategy resulted in erroneous results (not shown here), when the target RI values are not within  $\sim 35\%$  of the approximated values. The variations in RI for each region of breast reported in the literature is well within this range [90, 94, 97].

The results obtained using three fiber layer data are given in Table 4.2 with varying RI (given in the first column) for the RI-U strategy in the case of 1915 mesh. When compared to the estimated optical properties using single layer data (third row of Table 4.1), the errors have decreased by 4 times. But, they are still erroneous compared to RI-E and RI-A strategies (fourth and fifth row of Table 4.1). Among the uniform RI values (1.467, 1.4, and 1.33; in RI-U strategy) for the meshes considered in this chapter, RI value of 1.4 lead to lesser erroneous estimates of optical properties (also reflected in Table 4.2). When results obtained using RI-U strategy with RI = 1.4 compared against RI-E and RI-A strategies, the later strategies resulted in error reduction of atleast 30%. Note that a similar trend was observed for other meshes (not shown here), indicating that the assumption of uniform RI in the image-guided optical imaging of breast leads to inaccurate estimation of optical properties.

The simulation studies with multiple tumors (specifically breast having 4 regions with 2 of them being tumor region) were performed on the breast meshes. These results (not shown here) closely followed the observed trends of the case where breast had three regions (with only one tumor region).

Also, the estimated optical properties values did not change significantly (not more than  $\sim 5\%$ ) when the  $\lambda$  in Eq. 4.2 was varied from 0.01 to 1000, which is expected in the case of LM minimization with J being close to positive-definite (as  $NM \gg NR$ ) [40]. The effect of RI in traditional DOT is being explored currently as it requires development of computationally efficient techniques in the estimation of optical properties along with the new methodology for the estimation of RI.

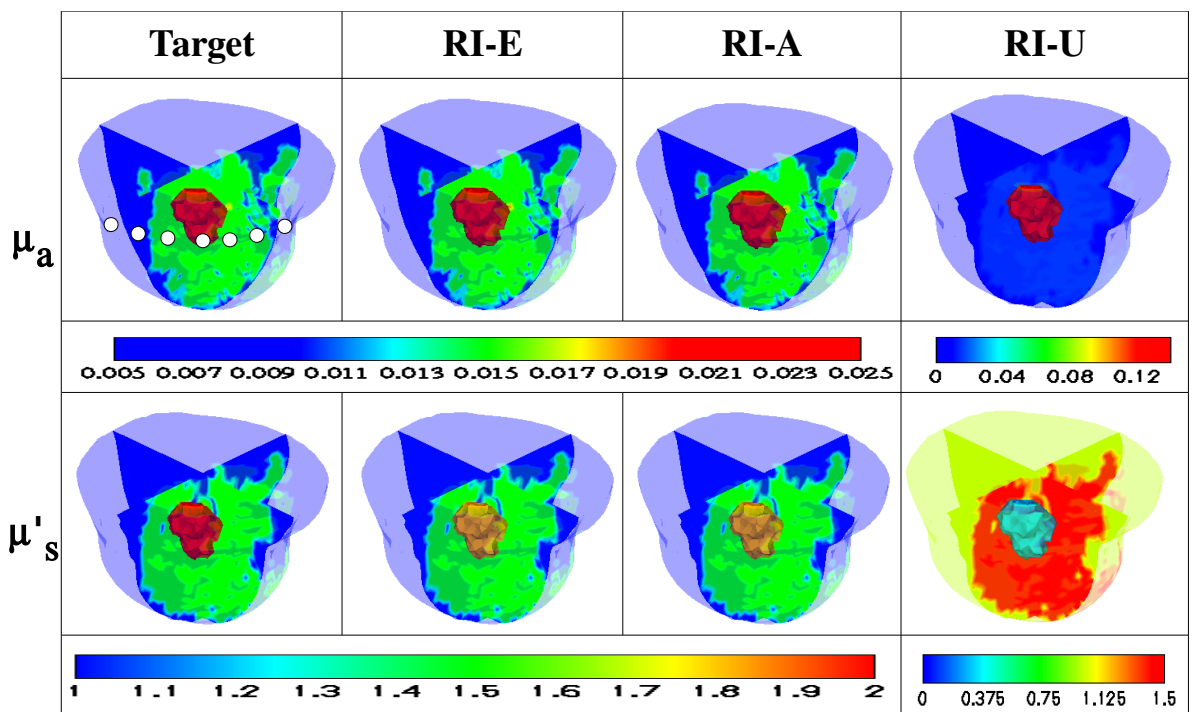


Figure 4.1: Reconstructed distributions of  $\mu_a$  (top row) and  $\mu'_s$  (bottom row) using the three strategies discussed in Sec. 4.2.2. (given on top of each column) along with the target distributions (first column) for 1915 mesh. The source/detector fibers are indicated by filled circles in the  $\mu_a$  distribution of the target. The estimated optical properties for this 1915 mesh are also listed in Table 4.1.

# Chapter 5

## Gradient-Free Simplex Method for IG-DOT

### 5.1 Introduction

The *hard-priors* (also known as IG-DOT) approach makes the diffuse optical image reconstruction problem less ill-posed compared to traditional approach (including *soft-priors*), due to the number of optical parameters to be reconstructed are far lesser compared to the number of measurements available. Specifically, this converts the problem from under-determined in nature to over-determined [98]. Even then the reconstruction procedures that are adapted in the *hard-priors* case are same as the ones used in the traditional approach with most popular one being *Levenberg-Marquardt* (LM) minimization scheme [43]. This LM scheme requires regularization parameter, which not only controls the convergence (number of iterations required) [101], some times leads to biased solutions. Moreover, the LM scheme that is typically adapted to diffuse optical imaging requires calculation of Jacobian (first-order derivative of the model), which is the most computationally expensive step of the image reconstruction procedure [73]. This chapter explains that a gradient-free simplex method [66, 74], which does not require regularization as well as computation of gradient (or its variant Jacobian), is highly efficient compared to the existing methods for solving the image reconstruction problem in

*hard-priors* approach. The reconstruction results using the proposed method have been compared with traditional methods using numerical and also gelatin phantom experimental cases.

## 5.2 Gradient-Free Simplex Method

The estimation of the optical absorption coefficients (in here, equal to number of regions) involves matching the experimentally measured boundary data ( $y$ ) iteratively with  $G(\mu_a)$  in a least-square sense by varying  $\mu_a$  in different regions [43]. The objective function that needs to be minimized with respect to  $\mu_a$  here is again the data-model misfit,  $\Omega(\mu_a) = \|y - G(\mu_a)\|^2$  where the dimension of  $y$  and  $\mu_a$  is given by M (number of measurements) and R (number of regions only) respectively. Even though,  $R \ll M$ , the minimization problem is still ill-posed (also non-linear), requiring regularization. The popular LM minimization scheme results in an update equation [43] given by  $\Delta\mu_a = [J^T J + \lambda I]^{-1} J^T \delta$ , where  $J^T$  represents the transposed Jacobian  $J (= \frac{\partial G(\mu_a)}{\partial \mu_a}$ , dimension:  $M \times R$ ),  $I$  is the identity matrix,  $[y - G(\mu_a)]$  is the data-model misfit,  $\Delta\mu_a$  is the update, and the regularization parameter is represented by  $\lambda$ . The  $\lambda$  is systematically decreased with each iteration, in here by a factor  $10^{0.25}$ . As  $J$  is known to be semi-positive definite in the case of *hard-priors* [43], the  $\lambda$  effects the convergence properties of the solution [101]. After every iteration, the  $\mu_a$  is updated by adding  $\Delta\mu_a$  followed by recomputing of  $J$  and  $G(\mu_a)$  are recomputed before proceeding to update equation. This procedure is repeated until the change in  $\Omega$  becomes less than 2% between successive iterations, ensuring the convergence of the solution.

### 5.2.1 Nelder and Mead simplex algorithm

As the convergence is dependent on  $\lambda$  for the LM minimization, a direct search method that can minimize a scalar-valued nonlinear function, such as  $\Omega$ , is Nelder and Mead simplex algorithm [66, 74]. This algorithm is extremely popular for the unconstrained minimization problem, which does not require explicit or implicit calculation of the

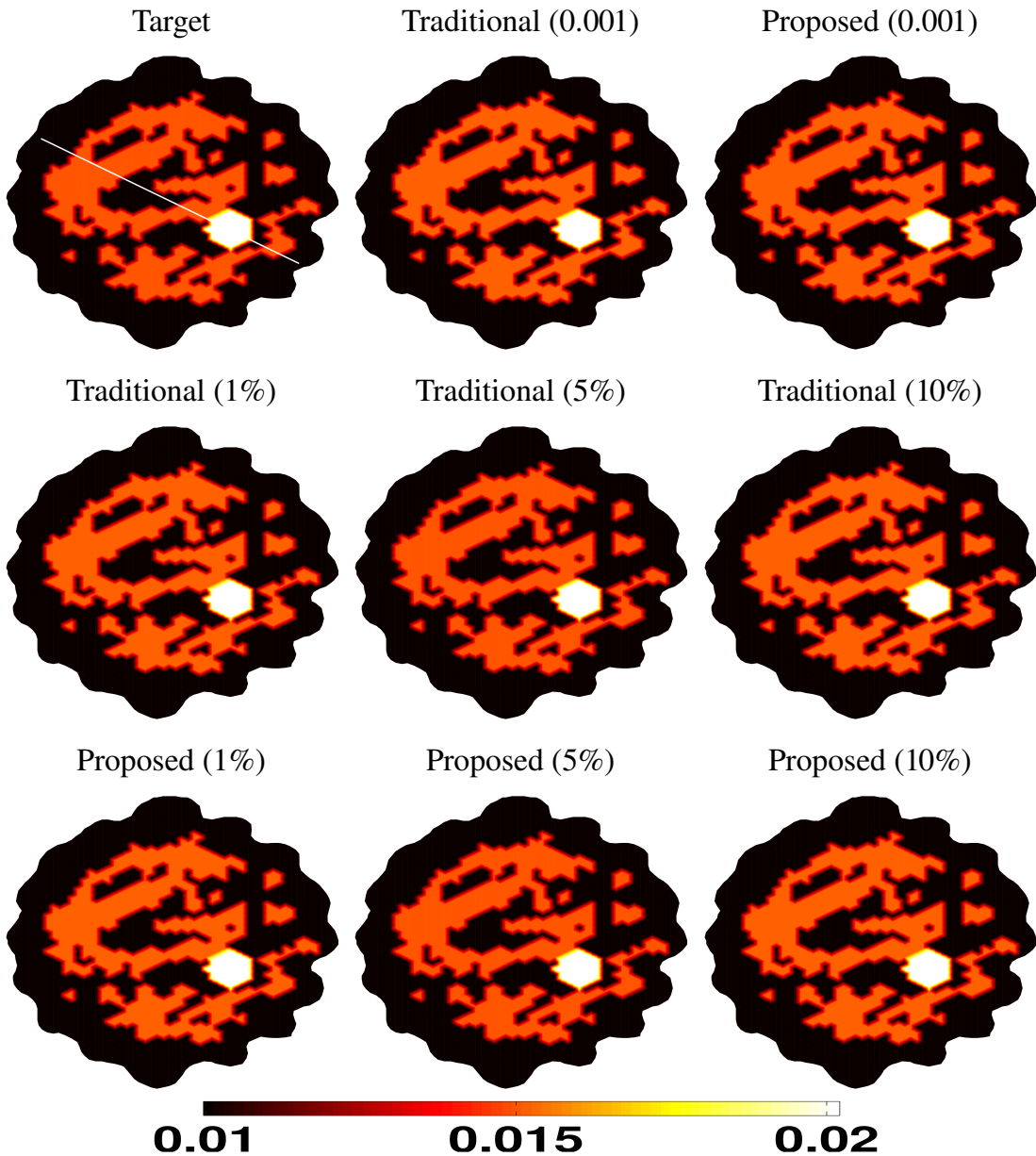


Figure 5.1: Comparison of reconstruction performance for the case of numerically generated data with 1% noise. The reconstruction techniques that were used are given on top of each figure, with the traditional being LM method, Proposed being the Nelder-Mead simplex method, and target represents actual  $\mu_a$  distribution. The initial guess for the top row is  $0.01 \text{ mm}^{-1}$  and for the bottom row it is  $0.001 \text{ mm}^{-1}$ .

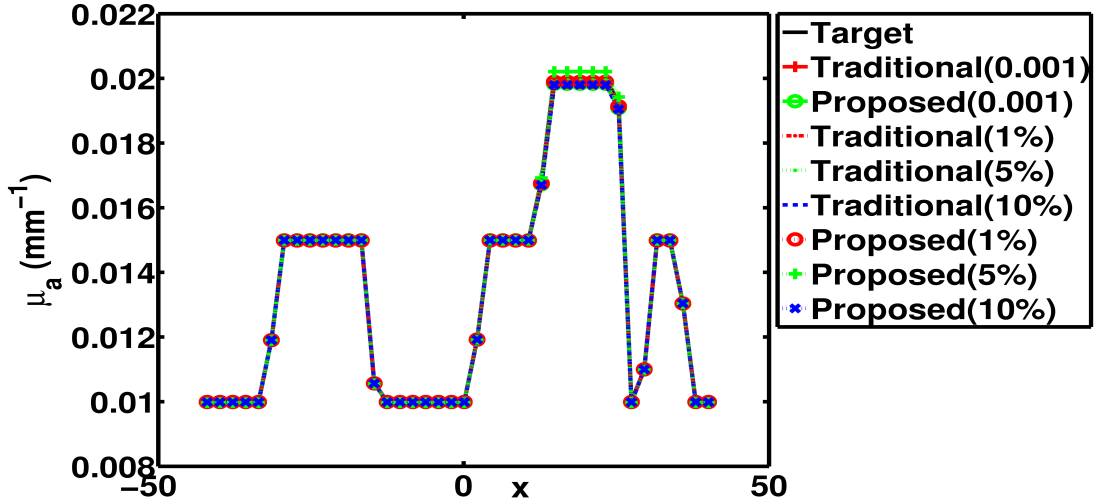


Figure 5.2: The one-dimensional cross-section plot along the dotted line on the target image (given at the top left corner of the Fig. 5.1) for all the reconstruction results shown in Fig. 5.1.

derivatives (or its variants gradients) [74], making it one of the most efficient technique. The only requirement for this algorithm is that it involves repeated calculation of  $G(\mu_a)$ . Since the objective function ( $\Omega$ ) has only  $R$  number of parameters, the direct search method forms the initial simplex with  $R + 1$  points, with each point having a dimension of  $R \times 1$  using the initial guess of  $\mu_a$ . These form the vertices of the simplex. The simplex method of minimization is achieved through series of steps that are deployed repeatedly. Let the maximum value of the objective function( $\Omega$ ) be at the point  $\mu_a^R$ , which is replaced by a new point  $\mu_a^r$  via *reflection*, i.e.

$$\mu_a^r = (1 + \alpha)\bar{\mu}_a - \alpha\mu_a^R \quad (5.1)$$

where  $\bar{\mu}_a$  represents the centroid of the the simplex and  $\alpha$  is the reflection coefficient (positive value, in here it is 1). If the  $\Omega(\mu_a^r)$  lies between  $\Omega(\mu_a^1)$  (lowest value) and  $\Omega(\mu_a^R)$  then  $\mu_a^r$  becomes the  $\mu_a$  and we terminate the iteration. Otherwise, if  $\Omega(\mu_a^r) < \Omega(\mu_a^1)$  then *expand* using

$$\mu_a^e = (1 + \chi)\bar{\mu}_a - \alpha\mu_a^R \quad (5.2)$$

where  $\chi$  is the expansion coefficient taking a value of 2. If  $\Omega(\mu_a^e) < \Omega(\mu_a^r)$ , then make  $\mu_a = \mu_a^e$ ; if  $\Omega(\mu_a^e) \geq \Omega(\mu_a^r)$  then  $\mu_a = \mu_a^r$  and terminate the iteration. In case *expand* condition is not satisfied, then the *contract* step is taken, similar to earlier  $\Omega$  using the contraction  $\mu_a$  is compared and updated [66]. This follows a *shrinkage* step [66]. The coefficients that are used here are 0.5 (contract) and 0.5 (shrinkage). Note that these coefficients are universally accepted [66] as the standard and fixed for the method proposed here. More details of the algorithm along with the flow chart and tie-breaking rules are given in Ref. [66]. The procedure is repeated until the change in the  $\mu_a$  between the successive iterations becomes less than  $10^{-12}$ . The simplex algorithm requires repeated computation of  $\Omega$ , in turn evaluates  $G(\mu_a)$  at every step, for converging to solution. This algorithm is known to be providing optimal solution, when the parameter space dimensionality is within the range of data space [66]. So the *hard-priors* method becomes a good case for deployment of this method.

### 5.3 Simulation Studies

To effectively asses the reconstruction performance of the proposed method, a numerical experiment involving a typical MRI-NIR human breast case is considered. The target distribution of the same is shown in the left top corner of the Fig. 5.1. The optical properties of the tissue types are  $\mu_a = 0.01 \text{ mm}^{-1}$  for the fatty region;  $\mu_a = 0.015 \text{ mm}^{-1}$  for fibro-glandular; and tumor with  $\mu_a = 0.02 \text{ mm}^{-1}$ . The  $\mu'_s$  is assumed to be known and kept constant at  $1 \text{ mm}^{-1}$  throughout the imaging domain. The boundary measurement are taken using the 16 light source-detector fiber optic bundles that are arranged in an equi-spaced manner along the edge; when one fiber delivers the light then rest act as detectors which provides  $M = 240$  measurements. The mesh used for the data collection is a fine mesh with 4876 nodes (9567 triangular elements) and 1% Gaussian noise is added to mimic the experimental case. For the reconstruction a coarse mesh with 1969 nodes (3753 triangular elements) was used. The reconstruction results using fatty region as initial guess is given on the top row of the Fig. 5.1. The bottom row shows the

reconstruction results with initial initial guess of  $0.001 \text{ mm}^{-1}$ , which is far away from the actual solution. The traditional method converges to solution in 3 iterations (1.9 sec) for the initial guess being close to actual solution (top-row) with  $\lambda = 0.01$ . If the  $\lambda = 100$  is used in this case, the convergence is achieved in 11 iterations taking 15.5 sec. For the proposed simplex method, total computation time is 2.7 sec (47 function evaluations). For the bottom row results, the computation time for the traditional LM method is 3.5sec with  $\lambda = 0.01$  and 12.8 sec for the proposed simplex method. The one-dimensional cross-sectional profile along the solid line shown on the target for all the reconstruction results is given in the next Fig. 5.2. The results obtained using the proposed simplex method are matching within 2% of results met were obtained using the traditional LM method.

## 5.4 Gelatin Phantom Study

The same experimental data as in Sec. 2.3.2 was used in here along with the necessary finite element meshes. The reconstructed distributions of  $\mu_a$  using both traditional LM and the proposed simplex methods were given in Fig. 5.3 along with the one-dimensional cross-sectional profiles. The number of iterations required for traditional method were 6 for  $\lambda = 1$ , requiring 3.1 seconds. For  $\lambda = 100$ , the convergence was achieved in 11 iterations, requiring 14.9 seconds. The proposed method computational time is 9.5 sec (180 function evaluations). This case also shows that the proposed method results are in close agreement with the ones obtained using traditional LM method.

Traditional methods of image reconstruction in DOT mainly uses the Tikhonov-minimization scheme which is a the least squares minimization technique and is a well known technique for large system of equations. This method can be applied for suitably wide range of values and also reduces the noise. But the main limitation is that it requires the regularization parameter and it is chosen based on prior experience. Hence it is different for each problem and introduces unavoidable bias to the solution. The

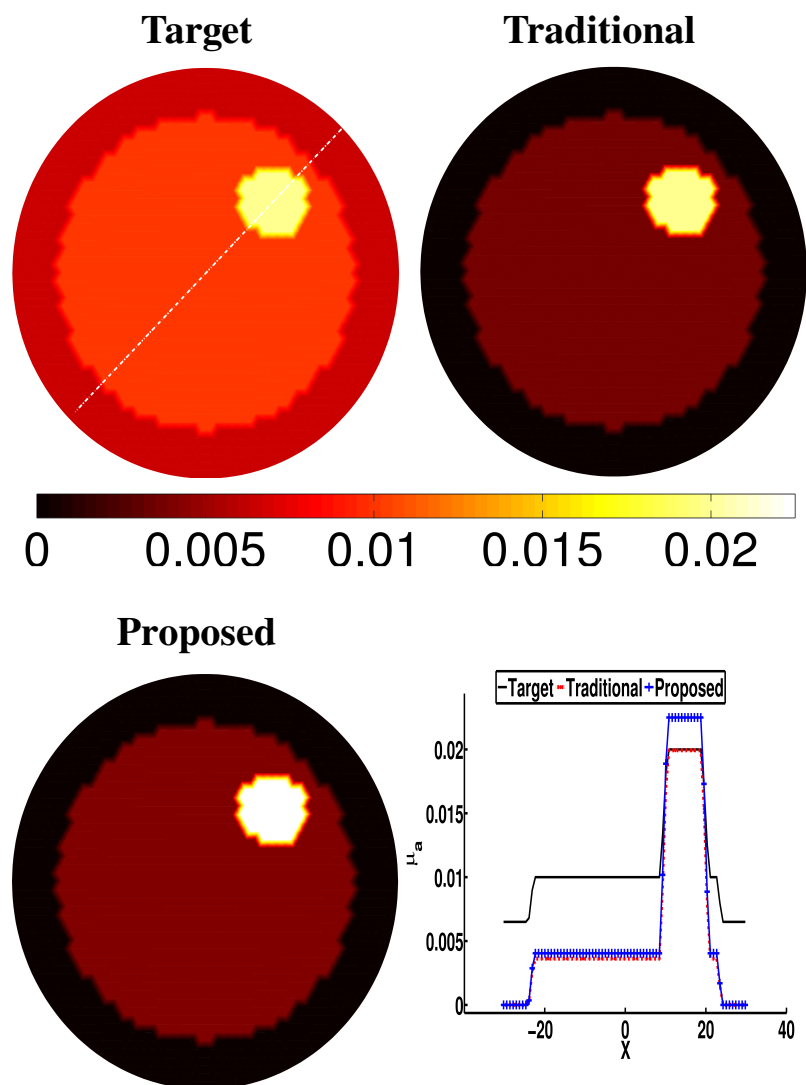


Figure 5.3: Similar effort as in Fig. 5.1 for the case of experimental gelatin phantom data. The initial guess here is obtained using the data-calibration procedure.

regularization parameter is to be chosen in the particular range, otherwise it may lead to solution which are far from reality. In LM method, if a larger value is used it will result in more number of iterative steps before the algorithm reaches the optimal solution, resulting in more computational time. Also the solution obtained depends on the regularization, lesser value promotes higher contrast in the reconstructed images and noise also amplified, whereas higher value leads to loss of resolution and smoothening of the solution. For the image-guided DOT, where the number parameters to be reconstructed is reduced to the number of the region segmented from the high resolution traditional imaging modalities, in this chapter a new method is proposed which is based on Nelder-Mead simplex algorithm. This simplex-algorithm [74] solves the unconstrained optimization of a non-linear functions without evaluating the derivatives of the function and hence, is independent of any heuristic inclusion on regularization parameter. The initial value for searching the optimal solution is obtained using the bulk properties of the breast tissue and the algorithm reaches the solution by solving the forward problem for about 100 times. The algorithm is independent of the initial guess and one such case is shown in Fig. 5.1 (first row), where the initial values are far away ( $0.001\text{ mm}^{-1}$ ) from the actual solution. The Newton-methods fails to converge to the solution, if it is not close to the solution. The proposed method is also tested for the cases where there is high noise and even in such cases the method finds the optimal solutions comparable with the traditional method.

In both numerical and gelatin phantom experiments, the total computational time that was reported for the traditional LM method was dependent on  $\lambda$ . The converged solution is same for cases when  $\lambda$  lies between 0.01 and 100, outside this range it is far away from actual solution. The proposed method does not require regularization, in turn, removing the unwarranted bias introduced in the solution in the traditional LM method. More importantly, the proposed method does not require/build any Jacobian, which might be a time-consuming process even for the image-guided diffuse optical tomography where the detection mechanism is based on CCD cameras resulting in  $M = 1e7$  [102].

# Chapter 6

## Conclusion

This thesis described mainly developments and algorithmic improvements in diffuse optical image reconstruction using limited boundary data. These improvements were made in both multi-modal and stand-alone diffuse optical image reconstruction algorithms. These developments primarily utilized the additional information available into the image reconstruction scheme more effectively to better estimate the optical properties.

The regularization parameter that is typically used in the diffuse optical tomographic image reconstruction procedure provides a fidelity in improving the reconstructed image quality, with a caveat that such fidelity can also bias the results. An automated estimation of regularization parameter that is based on regularized minimal residual method is presented in this work and is compared with the traditional GCV-based method. The reconstruction results using numerical and gelatin phantom data indicate that the proposed MRM based method can provide optimal regularization parameter overcoming the pit-falls of GCV-based method. Such automated method requires repeated computations of forward solutions and is not computationally complex compared to the direct image reconstruction step. The computer programs for the developed method that is used in this work are provided as open source.

For diffuse optical tomographic reconstruction, a new framework that can easily incorporate non-quadratic penalty terms was developed and through numerical and experimental phantom cases these penalization schemes were systematically compared with each other. The non-quadratic penalty terms that were used in this work include,  $\ell_1$ , Cauchy and Geman-McClure. The Generalized Cross-Validation method is also deployed in this work for automatic estimation of regularization parameter in each of these penalization schemes to remove any heuristics involved in the optical property estimation process. The results indicate that the non-quadratic penalization has advantages compared to traditional quadratic penalty in terms of improving the reconstructed image characteristics especially in cases where high contrast and complex shapes needs to be reconstructed.

Image-guided diffuse optical tomography (IG-DOT) image reconstruction was improved, in this thesis, by the inclusion of approximate variation of refractive index (RI) of the imaging media and was studied using realistic patient 3D breast meshes. It was shown that by assuming identical RI for different regions in breast could lead to erroneous estimation of optical properties. The *a-priori* knowledge of RI should lead to accurate estimation of optical properties. More importantly, in cases where it is not feasible to obtain the RI of different regions of breast, using even approximate values of RI for each region of breast could lead to better estimates of optical properties in IG-DOT. Even though this study presented here is pertained to breast imaging, the trends and observations made in this study should hold good for other IG-DOT studies as well, including brain imaging. In conclusion, effective usage of image guidance by incorporating the RI variation (by approximation) in the computational model has improved the estimation of optical properties in IG-DOT.

In this thesis, we have also proposed a new approach for IG-DOT image reconstruction that is based on popular gradient-free Nelder-Mead simplex method. The reconstructed optical property images were closely matching with the ones obtained using

traditional image reconstruction methods. Moreover, the proposed method removes the unwarranted bias introduced by the regularization that is typically needed in traditional methods.

These developments were more generic in nature for the inverse problems that have similar framework as diffuse optical tomography, making these easily adaptable to other scenarios such as diffuse fluorescence tomography, electrical impedance tomography, and electrical capacitance tomography.

Even though these developments are more efficient compared to the traditional methods, one could deploy high performance computing environment, such as Graphics Processing Units (GPUs), for massive parallelization and improving the computational run time of these algorithms. The developed algorithms are posted on the web as an open-source [61] and the details are given the Appendix-A.

# **Appendix A**

## **List of Packages/Programs**

This appendix gives the list of important MATLAB-based software packages and programs that were used/created as a part of this thesis work.

### **A.1 Packages**

The open-source MATLAB-based software packages that were used in this work are:

1. NIRFAST [Near Infrared Fluorescence and Spectral Tomography Software]
  - Link: <http://code.google.com/p/nirfast/>
  - Version: 7.1
  - Accessed on: Feb 12, 2012.
2. Regularization Tools
  - Link: <http://www2.imm.dtu.dk/~pcha/Regutools/>
  - Developed: Prof. Per Christian Hansen, Technical University of Denmark.
  - Version: 4.1
  - Accessed on: Feb 12, 2012.

## A.2 Developed Programs

A brief description of the developed programs are given in the table below and are available for download [63] at: <https://sites.google.com/site/sercmig/home/thesis-ravi-prasad/>.

Routine name and Description/Usage/Related Routines
<b>reconstruct_stnd_cw_OMRM.m</b> (Chapter 2) <i>Purpose:</i> Reconstruction routine using MRM-base regularization. <i>Usage:</i> reconstruct_stnd_cw_OMRM(fwd_mesh, data_fn, iteration, output_fn, filter_n), where the “ <i>fwd_mesh</i> ” represents the FEM mesh on which reconstruction is made using the experimental data “ <i>data_fn</i> ” and the output file is saved in “ <i>output_fn</i> ” after doing filtering and the type is represented by a the variable name “ <i>filter</i> ” . <i>Related Routines:</i> jacobian_stnd.m (NIRFAST), MRM.m and fminbnd.m (MATLAB)
<b>reconstruct_stnd_cw_GCV.m</b> (Chapter 2) <i>Purpose:</i> Reconstruction routine using GCV-based regularization. <i>Usage:</i> reconstruct_stnd_cw_first_frame(fwd_mesh, data_fn, iteration, output_fn, filter_n), where the items in parenthesis are same as in the first routine. <i>Related Routines:</i> jacobian_stnd.m (NIRFAST), TikGCVfun.m (Regularization Tools) and fminbnd.m (MATLAB)
<b>MRM.m</b> (Chapter 2) <i>Purpose:</i> Minimal Residual Method for solving the system of linear equation. <i>Usage:</i> MRM( $A, b, x_0, \alpha$ ),which solves a matrix equation $Ax = b$ with regularization “ $\alpha$ ” and the initial guess $x_0$ .

Routine name and Description/Usage/Related Routines
<p><b>reconstruct_cw_JtJ_Penalized_OGCV.m</b> (Chapter 3)</p> <p><i>Purpose:</i> Reconstruction routine using different GCV-based penalty terms.</p> <p><i>Usage:</i> reconstruct_cw_JtJ_Penalized_OGCV(fwd_mesh, data_fn, output_fn, iteration), where the items in parenthesis are same as in the first routine.</p> <p><i>Related Routines:</i> jacobian_stnd.m (NIRFAST) and TikGCVfun.m (Regularization Tools) .</p>
<p><b>reconstruct_cw_Opt_HardPrior.m</b> (Chapter 5)</p> <p><i>Purpose:</i> Reconstruction routine based on Nelder-Mead Simplex Algorithm.</p> <p><i>Usage:</i> reconstruct_cw_Opt_HardPrior(fwd_mesh, data_fn, iteration, output_fn, filter_n), where the items in parenthesis are same as in the first routine.</p> <p><i>Related Routines:</i> NelderMeadSimplexMethod.m and ObjectiveFunction_Opt_HardPrior.m</p>
<p><b>ObjectiveFunction_Opt_HardPrior.m</b> (Chapter 5)</p> <p><i>Purpose:</i> Evaluates the data-model misfit for the hard-prior reconstruction case and is used in the routine reconstruct_cw_Opt_HardPrior.m.</p> <p><i>Usage:</i> ObjectiveFunction_Opt_HardPrior(fwd_mesh, data_fn) where the “<i>fwd_mesh</i>” represents the FEM mesh (with region information) on which reconstruction is made using the experimental data “<i>data_fn</i>”.</p>
<p><b>NelderMeadSimplexMethod.m</b> (Chapter 5)</p> <p><i>Purpose:</i> Minimizes a real-valued function of several variables using Nelder-Mead Simplex algorithm.</p> <p><i>Usage:</i> NelderMeadSimplexMethod(fun, <math>x_0</math>) where “<i>fun</i>” represents the function handle of the multi-variable function to be minimized and the initial guess <math>x_0</math> for the minimizer.</p>

# References

- [1] American Cancer Society, *Cancer Facts and Figures 2012*, Atlanta: American Cancer Society, [www.cancer.org] (2012).
- [2] J. T. Bushberg, J. A. Seibert, E. M. Leidholdt, and J. M. Boone, *The essential physics of medical imaging*, Second Edition, Lippincott Williams and Wilkins, (2002).
- [3] B. Bone, Z. Pentek, L. Perbeck, and B. Veress, “Diagnostic accuracy of mammography and contrast enhanced MR imaging in 238 histologically veried breast lesions,” *Acta. Radiol.* **38**, 489–496 (1997).
- [4] S. J. Nass, I. C. Henderson, and J. C. Lashof, *Mammography and beyond: developing technologies for the early detection of breast cancer*, National Academy Press: Washington DC (2001).
- [5] M. F. Ernst and J. A. Roukema, “Diagnosis of non-palpable breast cancer: a review,” *The Breast* **11**, 13–21 (2002).
- [6] A. I. Mushlin , R. W. Kouides , and D. E. Shapiro, “Estimating the accuracy of screening mammography: a meta-analysis,” *Am J Prev Med.* **14**, 143-153 (1998).
- [7] C. L. Christiansen, F. Wang , M. B. Barton, W. Kreuter, J. G. Elmore, A. E. Gelfand, and S. W. Fletcher, “Predicting the cumulative risk of false-positive mammograms,” *J Natl Cancer Inst.* **92**, 1657–1666 (2000).

- [8] T. Hata, H. Takahashi, K. Watanabe, M. Takahashi, K. Taguchi, T. Itoh, and S. Todo, “Magnetic resonance imaging for preoperative evaluation of breast cancer: a comparative study with mammography and ultrasonography” *J. Am. Coll. Surg.* **198**, 190–197 (2004).
- [9] N. Hylton, “Magnetic Resonance Imaging of the breast: Opportunities to improve breast cancer management,” *J. Clin. Oncol.* **23**, 1678–1684 (2005).
- [10] Y. Chen, D. Tailor, X. Intes, and B. Chance, “Correlation between Near-Infrared spectroscopy (NIRS) and magnetic resonance imaging (MRI) on rat brain oxygenation modulation,” *Phys. Med. Biol.* **48**, 417–427 (2003).
- [11] E. S. Hwang, K. Kinkel, L. J. Esserman, Y. Lu, N. Weidner, and N. M. Hylton, “Magnetic resonance imaging in patients diagnosed with ductal carcinoma-in-situ: value in the diagnosis of residual disease, occult invasion, and multicentricity,” *Ann. Surg. Oncol.* **10**, 381–388 (2003).
- [12] M. Cutler, “Transillumination of breasts,” *Jour. of the Am. Med. Assoc.* **93**, 223–234 (1929).
- [13] C. M. Carpenter, B. W. Pogue, S. Jiang, H. Dehghani, X. Wang, K. D. Paulsen, W. A. Wells, J. Forero, C. Kogel, J. B. Weaver, S. P. Poplack, and P. A. Kaufman, “Image-Guided Optical Spectroscopy provides molecular-specific information in vivo: MRI-Guided Spectroscopy of breast cancer hemoglobin, water and scatterer size,” *Opt. Lett.* **32**, 933–935 (2007).
- [14] C. M. Carpenter, S. Srinivasan, B. W. Pogue, and K. D. Paulsen, “Methodology development for three-dimensional MR-guided near infrared spectroscopy of breast tumors,” *Opt. Exp.* **16**, 17903–17914 (2008).
- [15] R. Weissleder and V. Ntziachristos, “Shedding light onto live molecular targets,” *Nat. Med.* **9**, 123–128 (2003).

- [16] C. Balas, “Review of biomedical optical imaging a powerful, non-invasive, non-ionizing technology for improving *in vivo* diagnosis,” *Meas. Sci. Technol.* **20**, 104020–104032 (2009).
- [17] S. D. Konecky, *Non-invasive imaging of breast cancer with diffusing near-infrared light*, Dissertation in Physics and Astronomy, University of Pennsylvania (2008).
- [18] S. R. Arridge, M. Schweiger, M. Hiraoka, and D. T. Delpy, “A finite element approach for modeling photon transport in tissue,” *Medical Physics* **20**, 299–309 (1993).
- [19] D. A. Boas, D. H. Brooks, E. L. Miller, C. A. DiMarzio, M. Kilmer, R. J. Gaudette, and Q. Zhang, “Imaging the body with diffuse optical tomography,” *IEEE Sig. Proc. Mag.* **18**, 57–75 (2001).
- [20] S. R. Arridge and M. Schweiger, “Photon-measurement density functions. Part 2: Finite-element-method calculations,” *Appl. Opt.* **34**, 8026–8037 (1995).
- [21] M. Schweiger, S. R. Arridge, M. Hiroaka, and D. T. Delpy, “The Finite Element Model for the Propagation of Light in Scattering Media: Boundary and Source Conditions,” *Med. Phys.* **22**, 1779–1792 (1995).
- [22] S. R. Arridge, “Optical tomography in medical imaging,” *Inv. Problems* **15**, R41–R93 (1999).
- [23] H. Jiang, K. D. Paulsen, U. Osterberg, B. W. Pogue, and M. S. Patterson, “Optical image reconstruction using frequency domain data: simulations and experiments,” *J. Opt. Soc. Am. A* **13**, 253–266 (1996).
- [24] D. A. Boas, T. Gaudette, and S. Arridge, “Simultaneous imaging and optode calibration with diffuse optical tomography,” *Opt. Express* **8**, 263–270 (2001).
- [25] A. H. Hielscher and S. Bartel, “Use of penalty terms in gradient-based iterative reconstruction schemes for optical tomography,” *J. Biomed. Opt.* **6**, 183–192 (2001).

- [26] A. Tarantola, *Inverse Problem Theory and Methods for Model Parameter Estimation*, SIAM (2004).
- [27] M. J. Eppstein, D. E. Dougherty, D. J. Hawysz, and E. M. Sevick-Muraca, “Three-dimensional Bayesian optical image reconstruction with domain decomposition,” *IEEE Trans. Med. Imag.* **20**, 147–163 (2001).
- [28] J. C. Ye, C. A. Bouman, K. J. Webb, and R. P. Milane, “Nonlinear multigrid algorithms for Bayesian optical diffusion tomography,” *IEEE Trans. Imag. Process.* **10**, 909–922 (2001).
- [29] S. Srinivasan, B. W. Pogue, H. Dehghani, S. Jiang, X. Song, and K. D. Paulsen, “Improved quantification of small objects in near-infrared diffuse optical tomography,” *J. Biomed. Opt.* **9**, 1161–1171 (2004).
- [30] C. Lawler, W. A. Suk, B. R. Pitt, C. M. St. Croix, and S. C. Watkins, “Multimodal optical imaging,” *Am. J. Physiol. Lung Cell Mol. Physiol.* **285**, 269–280 (2003).
- [31] R. L. Barbour, H. L. Graber, J. W. Chang, S. L. S. Barbour, P. C. Koo, and R. Aronson, “MRI-guided optical tomography: Prospects and computation for a new imaging method,” *IEEE Comp. Sci. Eng.* **2**, 63–77 (1995).
- [32] M. Schweiger and S. R. Arridge, “Optical tomographic reconstruction in a complex head model using a priori region boundary information.” *Phys. Med. Biol.* **44**, 2703–2721 (1999).
- [33] G. Boverman, E. L. Miller, A. Li, Q. Zhang, T. Chaves, D. H. Brooks, and D. Boas, “Quantitative spectroscopic diffuse optical tomography of the breast guided by imperfect a priori structural information,” *Phys. Med. Biol.* **50**, 3941–3956 (2005).
- [34] V. Ntziachristos, X. H. Ma, and B. Chance, “Time-correlated single photon counting imager for simultaneous magnetic resonance and near-infrared mammography,” *Rev. Sci. Instrum.* **69**, 4221–4233 (1998).

- [35] B. Brooksby, S. Jiang, H. Dehghani, B. W. Pogue, K. D. Paulsen, J. Weaver, C. Kogel, and S. P. Poplack, "Combining near infrared tomography and magnetic resonance imaging to study in vivo breast tissue: implementation of a Laplacian-type regularization to incorporate magnetic resonance structure," *J. Biomed. Opt.* **10**, 1–10 (2005).
- [36] B. Brooksby, B. W. Pogue, S. Jiang, H. Dehghani, S. Srinivasan, C. Kogel, T. D. Tosteson, J. Weaver, S. P. Poplack, and K. D. Paulsen, "Imaging breast adipose and fibroglandular tissue molecular signatures using Hybrid MRI-Guided Near-Infrared Spectral Tomography," *Proc. Nat. Acad. Sci. U.S.A.* **103**, 8828–8833 (2006).
- [37] X. Intes, C. Maloux, M. Guven, B. Yazici, and B. Chance, "Diffuse optical tomography with physiological and spatial a priori constraints," *Phys. Med. Biol.* **49**, N155–N163 (2004).
- [38] B. Brooksby, H. Dehghani, B. W. Pogue, and K. D. Paulsen, "Near infrared (NIR) tomography breast image reconstruction with a priori structural information from MRI: algorithm development for reconstructing heterogeneities," *IEEE J. Sel. Top. Quantum Electron.* **9**, 199–209 (2003).
- [39] M. Guven, B. Yazici, X. Intes, and B. Chance, "Diffuse optical tomography with a priori anatomical information," *Phys. Med. Biol.* **50**, 2837–2858 (2005).
- [40] P. K. Yalavarthy, B. W. Pogue, H. Dehghani, and K. D. Paulsen, "Weight-Matrix Structured Regularization Provides Optimal Generalized Least-Squares Estimate in Diffuse Optical Tomography," *Med. Phys.* **34**, 2085–2098 (2007).
- [41] C. B. Shaw, "Development of novel reconstruction methods based on  $\ell_1$ -minimization for near infrared diffuse optical tomography" M.Sc.(Engg.) Thesis, Indian Institute Of Science (2012).
- [42] J. Prakash, "Automatic selection of hyper-parameters in diffuse optical tomographic image reconstruction" M.Sc.(Engg.) Thesis, Indian Institute Of Science (2013).

- [43] P. K. Yalavarthy, B. W. Pogue, H. Dehghani, C. M. Carpenter, S. Jiang, and K. D. Paulsen, “Structural information within regularization matrices improves near infrared diffuse optical tomography,” *Opt. Express* **15**, 8043–8058 (2007).
- [44] H. Dehghani, M. E. Eames, P. K. Yalavarthy, S. C. Davis, S. Srinivasan, C. M. Carpenter, B. W. Pogue, and K. D. Paulsen, “Near Infrared Optical Tomography using NIRFAST: Algorithms for Numerical Model and Image Reconstruction Algorithms, Communications in Numerical Methods in Engineering (Special Issue on Recent Advances in Computational Techniques for Biomedical Imaging) **25**, 711–732 (2009).
- [45] S. R. Arridge and J. C. Hebden, “Optical imaging in medicine: II. modelling and reconstruction,” *Phys. Med. Biol.* **42**, 841–853 (1997).
- [46] S. L. Jacques and B. W. Pogue, “Tutorial on diffuse light transport,” *J. Biomed. Opt.* **13**, 041302 (2008).
- [47] A. Gibson and H. Dehghani, “Diffuse Optical Imaging,” *Phil. Trans. R. Soc. A* **367**, 3055–3072 (2009).
- [48] A. P. Gibson, J. C. Hebden, and S. R. Arridge, “Recent advances in diffuse optical imaging,” *Phys. Med. Biol.* **50**, R1–R43, (2005).
- [49] H. Dehghani, S. Srinivasan, B. W. Pogue, and A. Gibson, “Numerical modelling and image reconstruction in diffuse optical tomography,” *Phil. Trans. R. Soc. A* **367**, 3073–3093 (2009)
- [50] H. Dehghani, M. E. Eames, P. K. Yalavarthy, S. C. Davis, S. Srinivasan, C. M. Carpenter, B. W. Pogue, and K. D. Paulsen, “Near Infrared Optical Tomography using NIRFAST: algorithms for numerical model and image reconstruction algorithms,” *Commun. Numer. Meth. Engng.* **25**, 711–732 (2009).
- [51] B. W. Pogue, T. McBride, J. Prewitt, U. L. Osterberg, and K. D. Paulsen, “Spatially

- variant regularization improves diffuse optical tomography,” *Appl. Opt.* **38**, 2950–2961 (1999).
- [52] B. W. Pogue, X. Song, T. D. Tosteson, T. O. McBride, S. Jiang, and K. D. Paulsen, “Statistical analysis of nonlinearly reconstructed near-infrared tomographic images: Part I Theory and Simulations,” *IEEE Trans. on Med. Imag.* **21**, 755–763 (2002).
- [53] G. Golub and U. von Matt, “A Generalized cross-validation for large-scale problems,” *J. Comput. Graph. Statist.* **6**, 1–34 (1997).
- [54] N. Nguyen, P. Milanfar, and G. Golub, “A computationally efficient superresolution image reconstruction algorithm,” *IEEE Trans. Image Processing* **10**, 573–583 (2001).
- [55] T. O. McBride, B. W. Pogue, S. Jiang, U. L. Osterberg, and K. D. Paulsen, “A parallel-detection frequency-domain near-infrared tomography system for hemoglobin imaging of the breast *in vivo*,” *Rev. Sci. Instr.* **72**, 1817–1824 (2001).
- [56] B. W. Pogue and M. Patterson, “Review of Tissue Simulating Phantoms for Optical Spectroscopy, Imaging and Dosimetry,” *J. Biomed. Opt.* **11**, 041102 (2006).
- [57] B. W. Pogue, K. D. Paulsen, H. Kaufman, and C. Abele, “Calibration of near infrared frequency-domain tissue spectroscopy for absolute absorption coefficient quantitation in neonatal head-simulating phantoms,” *J. Biomed. Opt.* **5**, 182–193 (2000).
- [58] P. C. Hansen, J. G. Nagy, and D. P. O’Leary, *Deblurring images: matrices, spectra, and filtering*, SIAM, Philadelphia, (2006)
- [59] P. C. Hansen, “Regularization tools version 4.0 for Matlab 7.3,” *Numerical Algorithms* **46**, 189–194 (2007).
- [60] M. S. Zhdanov, *Geophysical Inverse Theory and Regularization Problems*, Elsevier Science Publishers, Edition 1 (2002).
- [61] Web link: <https://sites.google.com/site/sercmig/home/regdot>

- [62] W. F. Cheong, S. A. Prahl, and A. J. Welch, "A review of the optical properties of biological tissues," *IEEE J. of Quan. Elec.* **26**, 2166–2185 (1990).
- [63] Web link: <https://sites.google.com/site/sercmig/home/thesis-ravi-prasad>
- [64] M. Schweiger, S. R. Arridge, and I. Nissila, "Gauss-Newton method for image reconstruction in diffuse optical tomography," *Phys. Med. Biol.* **50**, 2365–2386 (2005).
- [65] C. B. Shaw and P. K. Yalavarthy, "Effective contrast recovery in rapid dynamic near-infrared diffuse optical tomography using  $\ell_1$ -norm-based linear image reconstruction method," *J. Biomed. Opt.* **17**, 086009 (2012).
- [66] J. C. Lagarias, J. A. Reeds, M. H. Wright, and P. E. Wright, "Convergence properties of the Nelder-Mead simplex method in low dimensions," *SIAM Journal of Optimization* **9**, 112–147 (1998).
- [67] S. H. Katamreddy and P. K. Yalavarthy, "Model-Resolution Based Regularization Improves Near Infrared Diffuse Optical Tomography," *J. Opt. Soc. Am. A* **29**, 649–656 (2012).
- [68] M. E. Eames and H. Dehghani, "Wavelength dependence of sensitivity in spectral diffuse optical imaging: effect of normalization on image reconstruction," *Opt. Express* **16**, 17780 (2008).
- [69] F. Larusson, S. Fantini, and E. L. Miller, "Hyperspectral image reconstruction for diffuse optical tomography," *Biomed. Opt. Express* **2**, 946–965 (2011).
- [70] J. P. Culver, R. Choe, M. J. Holboke, L. Zubkov, T. Durduran, A. Slemp, V. Ntziachristos, B. Chance, and A. G. Yodh, "Three-dimensional diffuse optical tomography in the parallel plane transmission geometry: evaluation of a hybrid frequency domain/continuous wave clinical system for breast imaging," *Med. Phys.* **30**, 235–247 (2003).
- [71] T. Correia, A. Gibson, M. Schweiger, and J. Hebden, "Selection of regularization parameter for optical topography," *J. Biomed. Opt.* **14**, 034044 (2009).

- [72] J. Chamorro-Servent, J. Aguirre, J. Ripoll, J. J. Vaquero, and M. Desco, “Feasibility of U-curve method to select the regularization parameter for fluorescence diffuse optical tomography in phantom and small animal studies,” *Opt. Express* **19**, 11490–11506 (2011) .
- [73] J. Prakash, V. Chandrasekharan, V. Upendra, and P. K. Yalavarthy, “Accelerating frequency domain diffuse optical tomographic image reconstruction using graphics processing units,” *J. Biomed. Opt.* **15**, 066009:1–9 (2010).
- [74] J. A. Nelder and R. Mead, “A simplex method for function minimization,” *Oxford Journals The Computer Journal* **7**, 308–313 (1965).
- [75] J. W. Stayman and J. A. Fessler, “Spatially-variant roughness penalty design for uniform resolution in penalized-likelihood image reconstruction,” *Proceed. of Intern. Conf. on Img. Proc. (ICIP)* **2**, 685–689 (1998).
- [76] P. Zwartjes and A. Gisolf, “Fourier reconstruction with sparse inversion,” *Geophysical Prospecting* **55**, 199–221 (2007).
- [77] P. Charbonnier, L. Blanc-Feraud, G. Aubert, and M. Barlaud, “Deterministic Edge-Preserving Regularization in Computed Imaging,” *IEEE Trans. on Image Processing* **6**, 298–311 (1997).
- [78] R. Acar and C. R. Vogel, “Analysis of bounded variation penalty methods for ill-posed problems,” *Inverse Problems* **10**, 1217–1229 (1994).
- [79] M D. Sacchi, T. J. Ulrych, and C. Walker, “Interpolation and extrapolation using a high resolution discrete Fourier transform,” *IEEE Trans. on Signal Processing* **46**, 31–38 (1998).
- [80] R. P. K. Jagannath and P. K. Yalavarthy, “Minimal Residual Method Provides Optimal Regularization Parameter for Diffuse Optical Tomography,” *J. Biomed. Opt.* **17**, 106015:1–7 (2012).

- [81] N. Ducros, C. D. Andrea, A. Bassi, G. Valentini, and S. Arridge, “A virtual source pattern method for fluorescence tomography with structured light,” *Phys. Med. Biol.* **57**, 3811–3832 (2012).
- [82] J. Prakash and P. K. Yalavarthy, “A LSQR-type method provides a computationally efficient automated optimal choice of regularization parameter in diffuse optical tomography,” *Med. Phys.* **2013** (*in press*).
- [83] K. B. Flach, R. Kueres, W. Semmler, M. Kachelrie, and S. Bartling, “Constrained reconstructions for 4D intervention guidance,” *Phys. Med. Biol.* **58**, 3283–3300 (2013).
- [84] H. Niu, P. Guo, L. Ji, Q. Zhao, and T. Jiang, “Improving image quality of diffuse optical tomography with a projection-error-based adaptive regularization method,” *Opt. Express* **16**, 12423–12434 (2008).
- [85] N. Cao, A. Nehorai, and M. Jacob, “Image reconstruction for diffuse optical tomography using sparsity regularization and expectation-maximization algorithm,” *Opt. Express* **15**, 13695–13708 (2007).
- [86] M. Schweiger and S. R. Arridge, “Comparison of two- and three-dimensional reconstruction methods in optical tomography,” *Appl. Opt.* **37**, 7419–7428 (1998).
- [87] F. Gao, P. Poulet, and Y. Yamada, “Simultaneous mapping of absorption and scattering coefficients from a three-dimensional model of time-resolved optical tomography,” *Appl. Opt.* **39**, 588–600 (2000).
- [88] B. W. Pogue, S. Geimer, T. O. McBride, S. Jiang, U. L. Sterberg, and K.D. Paulsen, “Three-dimensional simulation of near-infrared diffusion in tissue: Boundary condition and geometry analysis for finite element image reconstruction,” *Appl. Opt.* **40**, 588–600 (2001).
- [89] B. J. Tromberg, B. W. Pogue, K. D. Paulsen, A. G. Yodh, D. A. Boas, and A. E. Cerussi, “Assessing the future of diffuse optical imaging technologies for breast cancer management,” *Med Phys.* **35**, 2443–2451 (2008).

- [90] F. P. Bolin, L. E. Preuss, R. C. Taylor, and R. J. Ference, “Refractive index of some mammalian tissues using a fiber optic cladding method,” *App.Opt.* **28**, 2297–2303 (1989).
- [91] A. M. Zysk, E. J. Chaney, and S. A. Boppart, “Refractive index of carcinogen-induced rat mammary tumors,” *Phys. Med. Biol.* **51**, 2165–2177 (2006).
- [92] B. J. Tromberg, O. Coquoz, J. B. Fishkin, T. Pham, E. R. Anderson, J. Butler, M. Cahn, J. D. Gross, V. Venugopalan, and D. Pham, “Non-invasive measurements of breast tissue optical properties using frequency-domain photon migration,” *Phil. Trans. R. Soc. Lond. B* **352**, 661–668 (1997).
- [93] H. Dehghani, B. Brooksby, K. Vishwanath, B. W. Pogue, and K. D. Paulsen, “The effects of internal refractive index variation in near-infrared optical tomography: a finite element modeling approach,” *Phys. Med. Biol.* **48**, 2713–2727 (2003).
- [94] H. Dehghani, B. A. Brooksby, B. W. Pogue, and K. D. Paulsen, “Effects of refractive index on near-infrared tomography of the breast,” *App. Opt.* **44**, 1870–1887 (2005).
- [95] T. Khan and A. Thomas, “Inverse problem in refractive index based optical tomography,” *Inv. Problems* **22**, 1121–1137 (2006).
- [96] B. Brooksby, S. Jiang, H. Dehghani, B. W. Pogue, K. D. Paulsen, C. Kogel, M. Doyley, J. B. Weaver, and S.P. Poplack, “Magnetic resonance guided near infrared tomography of the breast,” *Rev. Sci. Inst.* **75**, 5262–5270 (2004).
- [97] X. Wang, *Estimation of Effective Scatterer Size and Number Density in Near-Infrared Tomography*, Ph.D. Thesis, Dartmouth College (2007).
- [98] B. W. Pogue, S. C. Davis, F. Leblond, M. A. Mastanduno, H. Dehghani, and K. D. Paulsen, “Implicit and explicit prior information in near-infrared spectral imaging: accuracy, quantification and diagnostic value,” *Phil. Trans. R. Soc. A* **369**, 4531–4557 (2011).

- [99] B. W. Pogue, M. Testorf, T. McBride, U. Osterberg, and K. D. Paulsen, “Instrumentation and design of a frequency-domain diffuse optical tomography imager for breast cancer detection,” *Opt. Express* **1**, 391–403 (1997).
- [100] R. P. K.Jagannath and P. K. Yalavarthy, “Approximation of internal refractive index variation improves image guided diffuse optical tomography of breast,” *IEEE Trans. Biomed. Engg.* **57**, 2560–2563 (2010).
- [101] R. Aster, R. C. Aster, B. Borchers, and C. H. Thurber, *Parameter estimation and inverse Problems*, Elsevier (2005).
- [102] S. D.Konecky, G. Y. Panasyuk, K. Lee, V. Markel , A.G. Yodh, and J. C. Schotland, “Imaging complex structures with diffuse light,” *Opt. Express* **16**, 5048–5060 (2008).